Development of a High-Frequency Surface-Wave Radar Cross Section Model for Icebergs

by

©Bernard Ryan, B. Eng.

A thesis submitted to the School of Graduate Studies in partial fulfillment of the requirements for the degree of

Master of Engineering

Faculty of Engineering and Applied Science

Memorial University of Newfoundland

May, 2016

St. John's Newfoundland

Abstract

In this thesis, the first-order radar cross section (RCS) of an iceberg is derived and simulated. This analysis takes place in the context of a monostatic high frequency surface wave radar with a vertical dipole source that is driven by a pulsed waveform.

The starting point of this work is a general electric field equation derived previously for an arbitrarily shaped iceberg region surrounded by an ocean surface. The condition of monostatic backscatter is applied to this general field equation and the resulting expression is inverse Fourier transformed. In the time domain the excitation current of the transmit antenna is specified to be a pulsed sinusoid signal. The resulting electric field equation is simplified and its physical significance is assessed. The field equation is then further simplified by restricting the iceberg's size to fit within a single radar patch width. The power received by the radar is calculated using this electric field equation. Comparing the received power with the radar range equation gives a general expression for the iceberg RCS.

The iceberg RCS equation is found to depend on several parameters including the geometry of the iceberg, the radar frequency, and the electrical parameters of both the iceberg and the ocean surface. The RCS is rewritten in a form suitable for simulations and simulations are carried out for rectangularly shaped icebergs. Simulation results are discussed and are found to be consistent with existing research.

Acknowledgements

First and foremost, I would like to thank my supervisor Dr. Eric Gill, who first introduced me to high frequency radar, Maxwell's equations, and the exciting world of electromagnetism. I would also like to thank Dr. Gill for his guidance and encouragement throughout my masters studies. I will miss our discussions on this thesis' work and our chats about the fundamentals of physics and mathematics in general. Your suggestions have been invaluable in helping me complete my masters.

I am grateful for the financial support from several benefactors including, the Natural Sciences and Engineering Research Council of Canada (NSERC) for their Canada Graduate Scholarship, the Research and Development Corporation of Newfoundland and Labrador (RDC) for their Ocean Industries Student Research Award, and finally, graduate student support from an NSERC grant (#238263-2010) to Dr. Gill.

I would also like to thank my wonderful family and friends for their love and support throughout my masters studies. In particular, my Aunt Brenda and Uncle Michael, whose support and interest in my work has helped me through both my undergraduate and masters programs. Finally, my parents, whose constant encouragement, love, and home-cooked meals enabled me to finish my thesis. This work truly could not have been completed without them.

Table of Contents

List of Tables

List of Figures

Table of Symbols

The page numbers here indicate the place of first reference. The majority of the symbols used in this thesis are specified here. However, some intermediate variables are not explicitly referenced below. Their definitions are obvious from the context.

R : Represents the finite (iceberg) region (p. 5).

μ_0 : Magnetic permeability of free space (p. 5).

σ_1, σ_2 : Electrical conductivity of the iceberg and ocean media, respectively (p. 5).

ϵ_1, ϵ_2 : Electrical permittivity of the iceberg and ocean media, respectively (p. 5).

ω : Radian frequency (p. 10).

ω_0 : System operating radian frequency (p. 10).

$i(t)$: Time domain current excitation waveform (p. 10).

I_0 : Amplitude of current excitation waveform (p. 10).

j : $\sqrt{-1}$ (p. 10).

σ : Electrical conductivity (p. 15).

ϵ : Electrical permittivity (p. 15).

ϵ_0 : Electrical permittivity of free space (p. 15).

x_0 : Distance from the iceberg center to the radar (p. 15).

$h_R(\cdot)$, $h_z(\cdot)$: Heaviside functions (p. 15).

$\vec{E}$: Electric field vector (p. 17).

$\vec{D}$: Electric flux density (p. 17).

$\vec{H}$: Magnetic field vector (p. 17).

$\vec{B}$: Magnetic flux density (p. 17).

$\vec{J}$: Current density including conduction current density $\left(\vec{J}_c\right)$ and source current density $\left(\vec{J}_s\right)$ (p. 17-18).

ρ_f : Free electric charge density (p. 17).

I : Source current in frequency domain (p. 19).

Δ_ℓ : Vertical dipole antenna's length (p. 19).

$\delta(\cdot)$: Dirac delta function (p. 19).

E_z^{z+} : Electric field (vertical component) at height z^+ (p. 20).

k : Wavenumber of radiated signal (p. 20).

$\overset{xy}{*}$: Two-dimensional spatial convolution (p. 20).

ρ : Distance from origin to a point (x, y) (p. 20).

ρ_0 : Distance from radar to a point (x, y) (p. 20).

Δ_1, Δ_2 : Normalized surface impedances of iceberg and ocean media, respectively (p. 20).

$F_1(\cdot)$, $F_2(\cdot)$: Sommerfeld attenuation function for the iceberg and ocean media, respectively (p. 20).

η_{01}^2, η_{02}^2 : Square of the refractive index for the iceberg and

	ocean media, respectively (p. 21).
$\mathrm{erfc}(\cdot)$:	Complementary error function (p. 22).
p_1 :	Numerical distance term given by $-jk\frac{\Delta_1^2}{2}\rho$ (p. 22).
$\left(E_z^{z+}\right)_0$:	Electric field due to the source (p. 22).
$\left(E_z^{z+}\right)_1, \left(E_z^{z+}\right)_2$:	First-order and second-order electric fields, respectively (p. 22).
ρ_0' :	Distance from radar to a point (x', y') (p. 24).
$\mathcal{F}_t^{-1}(\ )$:	Inverse Fourier transform (p. 34).
$\overset{t}{*}$:	Time convolution (p. 34).
c :	Speed of light (p. 34).
η_0 :	Intrinsic impedance of free space (p. 34).
f_0 :	System operating frequency (p. 35).
T_r :	Pulse width of transmitted signal (p. 36).
k_0 :	Wavenumber corresponding to operating frequency f_0 (p. 37).
ϕ :	Angle between radar and point on the iceberg (p. 38).
$\rho_1(\phi)$:	Shortest distance ρ_0' from radar to a point on the iceberg for a given ϕ (p. 38).
$\rho_2(\phi)$:	Furthest distance ρ_0' from radar to a point on the iceberg for a given ϕ (p. 38).
$\rho_{\min}$:	Distance ρ_0' from radar to the closest point on the iceberg (p. 40).
$\rho_{\max}$:	Distance ρ_0' from radar to the furthest point on the iceberg (p. 40).
$t_{\min}$:	The first instant at which the backscattered field is non-zero (p. 41).

$t_{\max}$: The last instant at which the backscattered field is non-zero (p. 41).

t_0 : Amount of time for the transmitted signal to travel to the iceberg center and return (p. 41).

P_r : Power received by the radar (p. 44).

σ : Iceberg radar cross section (p. 44).

P_t : Power transmitted by the radar (p. 44).

G_t : Transmitter gain (p. 44).

G_r : Receiver gain (p. 44).

A_r : Effective aperture of the receive antenna (p. 45).

y_1, y_2 : Limits corresponding to the iceberg's dimensions for y (p. 50).

x_1, x_2 : Location of closest and furthest points from the origin of the iceberg for a given y (p. 50).

a : Half the side length of the iceberg parallel to the radar's look direction (p. 54).

b : Half the side length of the iceberg which is facing the radar, i.e. perpendicular to radar's look direction (p. 54).

A : Area of rectangular iceberg given by $4ab$ (p. 56).

ϵ_{r_1}, ϵ_{r_2} : Relative permittivity of iceberg and ocean, respectively (p. 56).

L : Side length of square iceberg (p. 57).

P : Perimeter of square iceberg (p. 61).

Chapter 1

Introduction

1.1 Research Rationale

Oceans cover approximately seventy-one percent of the Earth's surface [1]. It is not surprising then that the human race relies heavily on the oceans for its survival and continual growth as a species. Traditionally humans have used the oceans as a source of food and for transportation, a behaviour which has continued into the present. Now, massive amounts of goods are transported across the ocean, enabling international trade to flourish, and seafood is still a staple in people's diets in most parts of the world. In addition to food and transportation, the oceans are a major source of hydrocarbons including oil and natural gas.

Despite the benefits the oceans have provided, they pose a serious safety threat to all those operating on or beneath their surfaces. In more northern (and southern) latitudes there is the additional hazard of sea ice. Icebergs, in particular, can cause massive damage to marine vessels and offshore structures in the event of a collision. The sinking of the “RMS Titanic” is perhaps the most famous example of this. Although the Titanic's crew managed to spot the iceberg, there was not enough time to redirect the ship and avoid collision [2]. This tragedy demonstrated the importance of the early detection of icebergs while navigating ice-infested waters.

Today, the number of ships and offshore structures operating in the vicinity of icebergs is greater than ever before. As such, knowledge of the location, size, and paths of nearby icebergs is critical for ensuring safe operation of marine vessels. Obtaining this information early, while the icebergs are still far away, is not only useful for collision avoidance, but also from a planning and efficiency perspective. For example, drilling schedules for offshore oil and gas developments can be modified based on the path of icebergs in order to maximize the up-time of expensive drilling platforms. Hydrocarbon developments which make use of floating production storage and offloading (FPSO) vessels can assess the sizes of approaching icebergs and make decisions to either redirect icebergs, if possible, or disconnect the FPSO from subsea equipment and move to a safe location. In both cases, having an early warning as well as accurate details regarding the iceberg's size and path is crucial from both a safety and operational efficiency standpoint.

Given the importance of detecting and classifying icebergs, a variety of techniques is used to track them. One common method is the use of microwave radar. These radar systems can be installed directly on a ship or offshore structure and offer good range resolution for nearby objects. Although these radars are excellent at "seeing" icebergs which are close, their detection range is usually limited to the visible horizon. As a result, these systems have a maximum detection range on the order of tens of kilometers [3]. Furthermore, microwave radars can experience decreased accuracy in the presence of adverse weather conditions such as heavy rain.

Another common iceberg monitoring technique uses airplanes to perform ice reconnaissance flights over high traffic areas. In North America, the North American Ice Service (NAIS) compiles data on the location of icebergs. This method provides surveillance over a wide area, but is an inherently expensive endeavor. As a result continuous data for an area is not available. Satellite technologies such as synthetic aperture radar (SAR) can also be used to monitor icebergs. However, satellites also lack continuous coverage and their range resolution may not be sufficient depending on the iceberg size [3].

Another tool which may be used for the remote sensing of icebergs is high frequency surface wave radar (HFSWR). This type of radar operates in the high frequency (HF) band of 3 to 30 MHz. Unlike a microwave radar system, radiated signals from HFSWR systems are able to travel over the horizon. This characteristic drastically increases the detection range for HFSWR systems to upwards of 300 km [4], depending on radar operating parameters and ocean conditions. Furthermore, HFSWR is not as sensitive to weather conditions like heavy rainfall and can continuously collect data over a wide area in near real-time. These advantages over the previously mentioned iceberg monitoring techniques make HFSWR an attractive candidate for iceberg remote sensing.

For many years HFSWR has been used as a remote sensor of the ocean surface itself. A natural extension of this application is the detection of hard targets such as icebergs which reside on the ocean surface. Over the past sixty years, a significant amount of research on HFSWR has focused on modeling its interactions with the ocean surface and using these models to infer ocean related information such as surface currents. In contrast, efforts exploring its use as an iceberg remote sensor have been relatively limited. Beginning in the 1980's, Dr. John Walsh of Memorial University and his colleagues began to develop models for the radar cross section (RCS) of an iceberg [5]. An iceberg RCS is essentially a mathematical description of what an iceberg “looks” like to an HFSWR system. Once a RCS is obtained, simulations of the RCS may be performed to understand how parameters such as iceberg size, shape, and radar operating frequency affect the received signal backscattered from the iceberg.

Walsh’s work was a fundamental effort in analytically modelling iceberg RCSs. However, his approach effectively assumed a plane wave source for the transmit antenna of the HFSWR system, which cannot be realized in physical HFSWR systems. In practice, an HFSWR transmitter is typically excited by either a pulsed sinusoid or a frequency modulated continuous wave (FMCW) current waveform. Since the RCS is dependent on the type of excitation waveform used, Walsh’s model cannot be accurately compared against experimental data from HFSWR systems which use these excitation waveforms. As such, Walsh’s early efforts into iceberg RCS modelling must be further developed to allow for any transmitter excitation waveform to be used.

This thesis aims to expand Walsh’s approach for deriving an iceberg RCS to allow a transmitter excitation waveform to be explicitly specified. This technique will then be applied to obtain an iceberg RCS for an HFSWR system driven by a pulsed sinusoid excitation waveform. It is hoped that this research will provide an approach which can be used for future iceberg HFSWR research and will facilitate comparison between field data and analytical RCS models.

1.2 Literature Review

The starting point of the research presented in this thesis is the electric field equations derived by Walsh [5]. Under the assumption of a vertical dipole source antenna, Walsh derives the vertical component of the electric field backscattered from a finite region. This region is depicted in Figure 1.1. The finite region is indicated by R and is surrounded by a second medium which has differing electrical characteristics. With respect to the application of iceberg detection, the finite region represents the iceberg while the medium surrounding the iceberg is the ocean surface. There is also a third medium representing air which exists above the ocean and iceberg media.

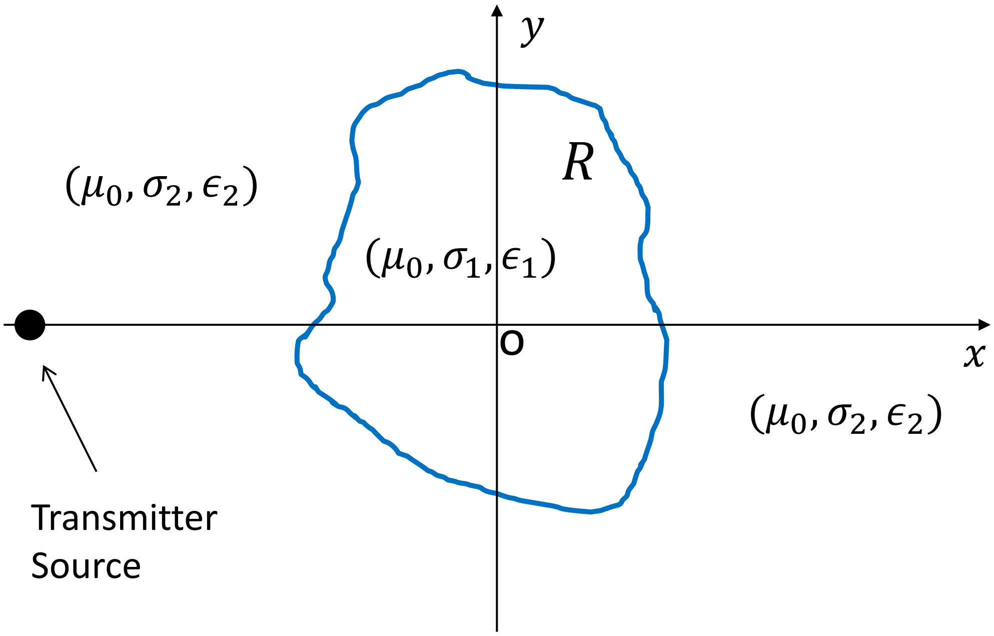

Figure 1.1: Finite (iceberg) region case

Before Walsh analyzes the finite (iceberg) region case of Figure 1.1, he first derives the electric field equations describing backscatter from a boundary separating two homogeneous media. This is referred to as the "simple discontinuity case" (Figure 1.2). The techniques used in deriving the simple discontinuity case are then adapted and applied to the finite region case to obtain a solution for the field backscattered off the region.

Walsh's work on the simple discontinuity case finds its roots in a category of

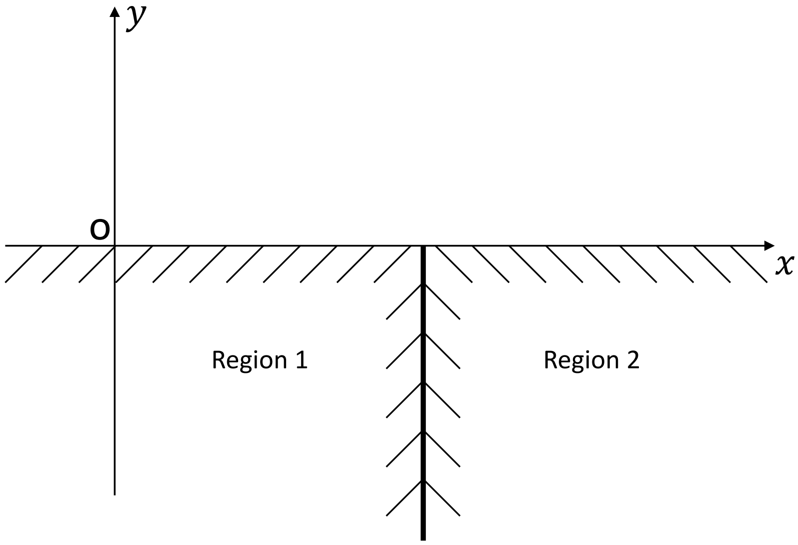

Figure 1.2: Simple discontinuity case

electromagnetic research referred to as “mixed path propagation”. Mixed path propagation problems involve the derivation of equations which describe electric fields as they propagate between regions with different electrical characteristics. A brief review of relevant research on the topic of mixed path propagation is given in Section 1.2.1. Literature covering the derivation of iceberg RCSs for HFSWRs is then detailed in Section 1.2.2.

1.2.1 Mixed Path Propagation Research

In the simple discontinuity case shown in Figure 1.2, the electromagnetic field generated by a source travels through region 1 and is incident on the discontinuity/boundary between the two regions. A portion of the incident field is transmitted past the boundary into region 2. This transmitted field, which exists only in region 2, is the so-called forward propagated field. The remainder of the incident field is reflected at the boundary and stays in region 1. This reflected field is called the backscattered field.

Research into mixed path propagation initially focused solely on the forward propagated field. In 1949, Millington [6] was the first to develop a method for calculating the field past a boundary. His work discusses ground wave propagation over an inhomogeneous smooth earth using an existing solution for propagation over a homogeneous smooth earth. This work predicted that as the field passed the boundary between a medium with lower conductivity to a medium with higher conductivity it would experience a recovery in field strength. As the field passed the boundary in the other direction a sharp decrease in strength was predicted. This phenomenon would later become known as the Millington recovery effect.

During the 1950's, Clemmow [7] and Bremmer [8] took two new approaches to the mixed path problem. Despite their differing techniques, in both works they obtained results consistent with those of Millington. Clemmow assumed there was a semi-infinite homogeneous flat medium with an infinitely thin perfectly conducting plane lying on top of one half of this homogeneous medium. Here the half-plane that had the conducting plane on top represents the second medium. Under the assumption of plane wave incidence, Clemmow then expresses the scattered field due to induced surface currents in the conducting sheet as a spectrum of plane waves which leads to dual integral equations. These integral equations are then solved using contour integration. Later Clemmow removes the perfectly conducting restriction on the second medium. Instead it is assumed that the modulus of the complex permittivity of each half-plane is large. Under this condition his work is shown to be consistent with that of Millington. Bremmer [8] uses a different approach to the same problem. His investigation of the propagation of radio waves over an inhomogeneous surface uses an integral equation based on Green's theorem. He finds solutions for the field close to the boundary and for the field far away from the boundary through the use of two-sided operational calculus. His solution to the integral equation is shown to be identical with Clemmow's work.

James Wait also carried out extensive work and publications on the topic of mixed path propagation and, in particular, the simple discontinuity case (see [9], [10], [11], and [12]). These works also agree about the forward propagated field, but like previous research they did not derive a description of the electric field backscattered from a simple discontinuity. In [13], Ryan analyzed the same model as Bremmer [8] and Wait [9], but in addition to deriving the field propagated past the boundary Ryan also derives an expression for the backscattered electric field. Ryan's analysis is based on a method of space/field decomposition which was originally demonstrated by Walsh in [14] and [15]. After showing that the forward propagated field derived is consistent with Bremmer's and Wait's work, Ryan finds the backscattered electric field equation and uses this equation to find the RCS expression of the simple discontinuity. Ryan's work in obtaining the backscattered electric field and RCS is especially useful from a practical perspective since a typical radar system will only receive signals which reflect off the region of interest and return to the radar.

In [13] Ryan also explores the concept of using HFSWR for ice-edge detection. The RCS derived by Ryan is general in the sense that no assumptions have been made regarding what the two media actually are. By substituting the values of the electrical characteristics (permittivity, permeability, and conductivity) for physically real media the effect on the RCS can be analyzed. In particular Ryan is interested in assessing the feasibility of HFSWR for ice edge detection so it is assumed that the first medium is sea water while the second medium is sea ice. Using his derived RCS expression he is able to determine the strength of the signal received by the radar and compare this against receiver noise. Ice edge detection is possible when the received signal from the ice edge is greater than the receiver's noise. Ryan carries out this analysis for different types of sea ice and even also considers sea ice to sea ice transitions. As such, this work, along with its associated papers [16], [17], and also [15] are some of the first modeling efforts for HFSWR ice detection.

1.2.2 Research on Iceberg RCS for HFSWR

The first significant modeling efforts of an iceberg RCS for HFSWR were carried out by Walsh [5] and by Walsh and Srivastava [18]. As previously discussed, Walsh first focuses on the simple discontinuity case shown in Figure 1.2. This analysis draws heavily on earlier work carried out by Walsh and Ryan [13], [15], [16]. As such, the same space/field decomposition technique used in these works is again employed for the electric field derivation. One benefit of this technique is that the boundary conditions arise naturally as part of the analysis. This is in contrast to the approaches Wait and Bremmer used where the boundary conditions had to be externally applied. Despite this, the boundary conditions derived by Walsh are the same as those assumed by Wait and Bremmer. Moreover, the forward propagated field derived by Walsh is also consistent with Wait [9], Bremmer [8], and Ryan [13]. The backscattered field is the same field equation found by Ryan.

After verifying the forward and backscattered field equations for the simple discontinuity case, Walsh next analyzes the finite region case depicted in Figure 1.1. His analysis for this case uses an adapted version of the methods used in the simple discontinuity case. In Walsh's derivation the excitation current waveform for the radar's transmit antenna is not explicitly specified. The derivation is carried out completely in the Fourier transform, or frequency, domain where the excitation current is assumed to be constant with respect to frequency. Although the current waveform is not explicitly assumed, Walsh later evaluates the electric field at the radian frequency $\omega = \omega_0$. It is possible to show that evaluating the field at ω_0 in the frequency domain is equivalent to assuming a time domain current with the form $i(t) = I_0 e^{j\omega_0 t}$, which is the expression for a plane wave excitation current with amplitude I_0 and radian frequency $\omega = \omega_0$. As a result, Walsh effectively assumes the current source to be a plane wave source. As noted previously, a plane wave current excitation is an ideal radiation source which cannot be realized in physical HFSWR systems.

In 1984, Walsh and Srivastava [18] produced a subsequent report to Walsh's work in [5]. Here the derivation continues from [5] to find the backscattered electric field for the finite region. This equation is then used to obtain a RCS for this region. Using the RCS equation, simulations are performed under the assumption that the finite region has the electrical properties of an iceberg with the surrounding medium being that of sea water. Two different iceberg shapes are considered: 1) a square iceberg and 2) an elliptical iceberg. The effect of shape and size on the RCS is investigated and detectable range is also discussed.

The iceberg RCS model developed by Walsh and Srivastava was compared against measurements from an actual radar system in 1986 [19]. Field measurements were carried out at Byron Bay, Labrador using an HFSWR system operating at 25.40 MHz. Using ground truth information for icebergs in the radar's detectable range, simulated RCSs were developed and compared against received data. While a small sample size of four icebergs was used, good agreement was demonstrated between the received and predicted signal-to-noise power density ratio. This paper helped to establish the feasibility of using HFSWR to remotely detect icebergs.

In the early 1990s, additional field data were collected at two HFSWR facilities located in Newfoundland and Labrador. The results of these field experiments are summarized in [3]. The first of these field tests took place at a facility in Cape Bonavista. Good results were demonstrated between actual field data and simulated results which were generated using software based on the iceberg RCS developed by Walsh and Srivastava. This was the case even though a different excitation waveform was used to drive the transmit antenna than the continuous sinusoid waveform assumed in the RCS derivation. However, a small but constant difference in the absolute level between the received and simulated signal peaks was noticed. The second set of field measurements were taken in Cape Race, Newfoundland. In this experiment, a comparison between the RCS model and field data was not carried out. However, several icebergs were detected and their radar determined locations were shown to agree with ship sightings.

Although the above-mentioned sets of field experiments helped to demonstrate the feasibility of HFSWR for iceberg detection and tracking, there has been little in the way of new analytical modelling of iceberg RCSs since that appearing in [19]. There was, however, a large effort put forth by Walsh and his colleagues to develop and interpret RCS models of the ocean surface itself. The methods developed for deriving ocean surface RCSs (see, for example, [20], [21], and [22]) allow for the substitution of any time domain excitation current waveform. Once an excitation waveform is explicitly specified, a RCS unique to the chosen excitation waveform can be obtained. These works provide a blueprint for generalizing Walsh's iceberg RCS research to account for any excitation waveform.

1.3 Scope of Thesis

As was discussed in Section 1.1, the primary goal of this thesis is to expand on existing iceberg RCS models to allow any type of excitation current waveform to be used as a transmitter source. In this thesis, the derivation carried out by Walsh in [5] is modified to allow a time domain excitation current to be explicitly chosen. Although any current waveform may be used as a transmit antenna source, a pulsed sinusoid waveform is assumed and the resulting backscattered first-order field equation is found. This equation is then simplified and used to obtain the RCS of an iceberg. Simulations regarding the effect of the iceberg's shape, size, and system operating frequency on the RCS are carried out and discussed.

The following chapter contains an overview of the general electric field equation developed by Walsh in [5] for a finite (iceberg) region. The chapter begins with the formulation of the finite region problem and then briefly discusses some of the major assumptions of Walsh's derivation. The electric field expression found by Walsh is separated into first-order and second-order components which are shown to represent physically different scattering mechanisms.

In Chapter 3 the first-order component is analyzed at length under the assumption of a monostatic radar configuration. In particular an inverse Fourier transform is performed on the backscattered field bringing the equation to the time domain. There it is converted to a form which allows any time domain excitation current waveform to be assumed. A pulsed sinusoid waveform is chosen for the RCS derivation and analysis. After inserting this current waveform, the backscattered electric field is simplified and coordinate transformed. A physical interpretation of the resulting equation demonstrates that the derived expression is consistent with the result expected for first-order scattering of a pulsed signal. By assuming that the iceberg's size fits within the patch width associated with the signal pulse, the backscattered field equation is further simplified and used to calculate the power received by the radar. The received power is then compared against the standard monostatic radar range equation resulting in a general expression for the iceberg RCS.

In Chapter 4, the iceberg RCS expression is first modified into a form suitable for simulation. Next, RCS simulation results are presented in order to gain an understanding of the effect that parameters such as iceberg shape, iceberg size, and system operating frequency have on the magnitude of the iceberg RCS. These results are discussed and are compared with previous iceberg RCS research.

In Chapter 5, the main conclusions found in the previous three chapters are summarized. This chapter also offers suggestions for future research in the area of HFSWR iceberg detection.

Chapter 2

Problem Formulation

The starting point of the research presented in this thesis is a general electric field expression obtained by Walsh in [5] for the finite region (iceberg) case. In order to provide a context for the origin of this expression, an overview of Walsh's derivation is first presented in this chapter. Sections 2.1 and 2.2, in particular, contain a description of the formulation of Walsh's analysis, highlighting the finite region model and also the first steps of his derivation. Section 2.3 then contains details of the electric field equation found by Walsh. That equation is separated into three different field components. In Section 2.4, these field components are interpreted in terms of physical scattering. Here it is shown that the total backscattered electric field is made up of both a first-order and second-order component, with the former being the focus of this thesis.

2.1 Space Decomposition

The three-dimensional space shown in Figure 2.1 is the starting point of this derivation. The figure shows a view of an iceberg as if looking down from above (the positive z axis is coming out of the page). The iceberg is the region denoted R, which has permeability, conductivity, and permittivity of μ_0, σ_1, ϵ_1, respectively. The region above the iceberg ($z > 0$) is assumed to be free space and has corresponding electrical parameters μ_0, $\sigma = 0$, ϵ_0. Surrounding the iceberg region is a medium representing the ocean surface which has electrical characteristics given by, μ_0, σ_2, ϵ_2. To simplify the analysis, both the ocean and the iceberg media are assumed to extend to infinity in the negative z direction. Also shown in Figure 2.1 is the transmitting antenna which is represented by an electrical source located at point $(x, y) = (-x_0, 0)$ and slightly above the ocean surface at $z = 0^+$. At this stage of the analysis the source is completely arbitrary and has not been specified. In Section 2.3.1 this source will be assumed to be a vertical dipole antenna.

For convenience the electrical parameters ϵ, σ, and μ for the entire space may be written in terms of the following Heaviside functions:

$$h_R(x, y) = \begin{cases} 1, & x, y \text{ in } R \\ 0, & \text{otherwise} \end{cases} \tag{2.1}$$

$$h_z(z) = \begin{cases} 1, & z > 0 \\ 0, & z \leq 0 \ . \end{cases} \tag{2.2}$$

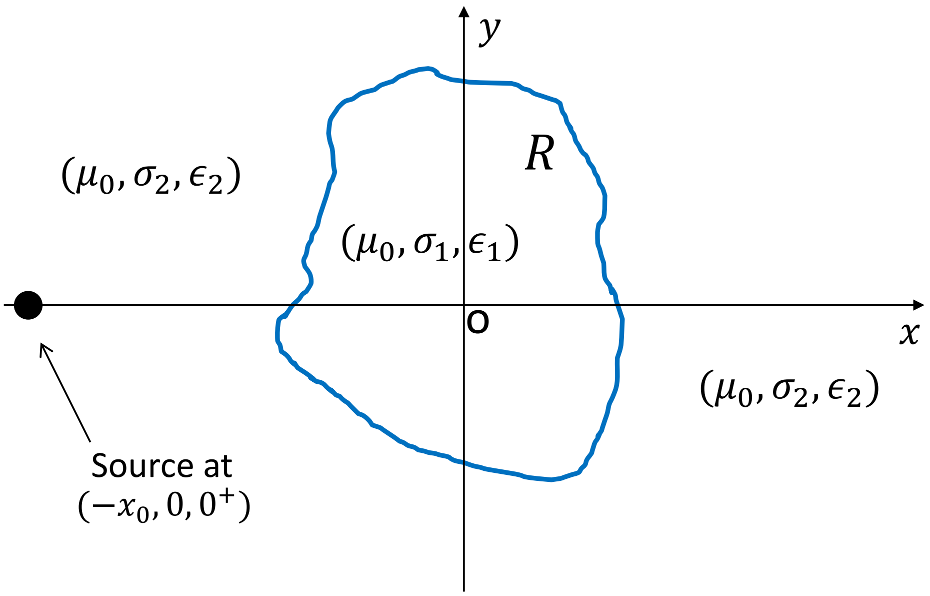

Figure 2.1: Space under analysis (top view)

Then,

$$\epsilon = \epsilon_0 h_z + (1 - h_z) \cdot \{\epsilon_1 h_R + \epsilon_2 (1 - h_R)\} \tag{2.3}$$

$$\sigma = (1 - h_z) \cdot \{\sigma_1 h_R + \sigma_2 (1 - h_R)\} \tag{2.4}$$

$$\mu = \mu_0 \tag{2.5}$$

where

ϵ = electrical permittivity

σ = electrical conductivity

μ = magnetic permeability

ϵ_0 = electrical permittivity of free space

μ_0 = magnetic permeability of free space.

2.2 Application of Maxwell's Equations

With an aim of obtaining an expression for the electric field, Maxwell's equations are now applied to the entire space in Figure 2.1. Maxwell's equations for the space may be written as:

$$\nabla \times \vec{E} = -j\omega\vec{B} \tag{2.6}$$

$$\nabla \times \vec{H} = j\omega\vec{D} + \vec{J} \tag{2.7}$$

$$\nabla \cdot \vec{B} = 0 \tag{2.8}$$

$$\nabla \cdot \vec{D} = \rho_f \tag{2.9}$$

where

$\vec{E}$ = Electric field vector

$\vec{B}$ = Magnetic flux density

$\vec{H}$ = Magnetic field vector

$\vec{D}$ = Electric flux density

$\vec{J}$ = Electric current density

ρ_f = Free electric charge density

ω = Radian frequency

$j = \sqrt{-1}$.

Here, Maxwell's equations are given in their time harmonic or Fourier transform with-respect-to-time form. As such equations (2.6) - (2.9) are a function of radian frequency ω. The electric current density, $\vec{J}$, is the sum of the conduction current density, $\vec{J}_c$, and the source electric current density, $\vec{J}_s$, i.e.

$$\vec{J} = \vec{J}_c + \vec{J}_s\,. \tag{2.10}$$

Under the assumption of point isotropy, the constitutive relationships take the following form:

$$\vec{B} = \mu\vec{H} \tag{2.11}$$

$$\vec{D} = \epsilon\vec{E} \tag{2.12}$$

$$\vec{J}_c = \sigma\vec{E} \tag{2.13}$$

where ϵ, σ, and μ are given by equations (2.3), (2.4), and (2.5), respectively.

2.3 Vertical Component of the Electric Field for an Iceberg

After applying Maxwell's equations to the space in Figure 2.1, Walsh begins to simplify the equations through the use of vector calculus and vector identities. Since the goal of this analysis is an expression for the backscattered electric field from an iceberg, Walsh solves for the electric field vector $\vec{E}$ (or, equivalently, $\vec{D}$ since $\vec{D} = \epsilon\vec{E}$) in equations (2.6) through (2.9). This is not a trivial task as the resulting mathematics are quite complex. However, the problem may be simplified because a complete description of $\vec{E}$ is not necessary. With reference to Figure 2.1 it may be noted that the source, which is the transmitting antenna, is located in the upper half space where $z > 0$. The location of the receiving antenna has not yet been specified but it must be in the upper half space since the lower half space represents the ocean. Since the field backscattered from the iceberg will be observed at the receiving antenna, a description of the electric field for only $z > 0$ is necessary. The problem is further simplified by noting that the field at the receiving antenna does not need to be determined for all $z > 0$ but only at the height of the antenna, i.e. at $z = z^+$ as z^+ approaches 0. Thus, the problem of finding $\vec{E}(x, y, z)$ for all x, y, z has been reduced to finding $\vec{E}(x, y, z^+)$.

2.3.1 Assumption of a Vertical Dipole Source

Obtaining an expression for the electric field $\vec{E}(x, y, z^+)$ requires a description of the field for each of its vector components $\hat{x}$, $\hat{y}$, $\hat{z}$. However, in practice, HFSWR systems make use of vertically polarized radiation. This is because surface wave propagation over the ocean severely attenuates the horizontal component of the electric field [23], [24]. As a result, the arbitrary source shown in Figure 2.1 is modelled as a vertical dipole antenna. Initially, Walsh keeps the electric field equations as general as possible by not explicitly specifying the form of the source. It is only later in the analysis that the source is assumed to be a vertical dipole.

Referring to (2.10), the source current density, $\vec{J_s}$, for a vertical dipole antenna is specified by Walsh as,

$$\vec{J_s} = I\Delta\ell\,\delta(x + x_0)\delta(y)\delta(z - a)\hat{z} \tag{2.14}$$

where I is the source current which is a function of radian frequency ω, and $\Delta\ell$ is the dipole antenna's physical length. It is clear that the delta (δ) functions in (2.14) indicate the physical location of the source antenna since $\vec{J_s}$ is non-zero only for $(x, y, z) = (-x_0, 0, a)$. The a term implies that the source is located at some finite height above the $z = 0$ boundary. However, this would be inconsistent with Figure 2.1 which shows the source is at a height $z = 0^+$ just above the boundary. After specifying the source current density to be that of (2.14) Walsh then assumes that a approaches 0 along the positive z-axis, which yields a result consistent with Figure 2.1.

2.3.2 Electric Field Equations

With the source being specified as a vertical dipole antenna, the analysis may now be restricted to a determination of the vertical component of the electric field. Instead of deriving an expression for the vector quantity $\vec{E}(x, y, z^+)$, only the z-component, $E_z(x, y, z^+)$, is required. In the ensuing analysis, this will be written as $E_z^{z+}(x, y)$. The mathematical analysis for finding E_z^{z+} is still quite involved, but restricting the scope to only the vertical component of the field at the height of the receive antenna greatly simplifies the process. In [5] Walsh finds the field equations for E_z^{z+} to be given by,

$$\begin{aligned} h_R E_z^{z+} = h_R \cdot \frac{I\Delta\ell k^2}{j\omega\epsilon_0(2\pi)} \Bigg[& F_2(\rho_0)\frac{e^{-jk\rho_0}}{\rho_0} \\ & + \frac{jk(\Delta_2 - \Delta_1)}{2\pi} \cdot \left(F_1(\rho)\frac{e^{-jk\rho}}{\rho} \right) \overset{xy}{*} \left(h_R \cdot F_2(\rho_0)\frac{e^{-jk\rho_0}}{\rho_0} \right) \Bigg] \end{aligned} \tag{2.15}$$

and

$$
\begin{aligned}
(1-h_R)E_z^{z+} = (1-h_R)\frac{I\Delta\ell k^2}{j\omega\epsilon_0(2\pi)}\Bigg[& F_2(\rho_0)\frac{e^{-jk\rho_0}}{\rho_0} \\
& + \frac{jk(\Delta_2-\Delta_1)}{2\pi}\cdot\left(F_2(\rho)\frac{e^{-jk\rho}}{\rho}\right)\overset{xy}{*}\, h_R\left\{F_2(\rho_0)\frac{e^{-jk\rho_0}}{\rho_0}\right. \\
& \left.+ \frac{jk(\Delta_2-\Delta_1)}{2\pi}\cdot\left(F_1(\rho)\frac{e^{-jk\rho}}{\rho}\right)\overset{xy}{*}\left(h_R\cdot F_2(\rho_0)\frac{e^{-jk\rho_0}}{\rho_0}\right)\right\}\Bigg] \qquad (2.16)
\end{aligned}
$$

with

$$
\begin{aligned}
\rho &= \sqrt{x^2+y^2} \\
\rho_0 &= \sqrt{(x+x_0)^2+y^2}\,.
\end{aligned}
$$

Here, k is the wavenumber of the radiation, $\overset{xy}{*}$ represents a two-dimensional spatial convolution in x and y, and Δ_1, Δ_2 are the normalized surface impedances of the iceberg and the ocean surface media, respectively. These surface impedances have the following form,

$$\Delta_1 = \frac{\sqrt{\eta_{01}^2-1}}{\eta_{01}^2} \qquad (2.17)$$

$$\Delta_2 = \frac{\sqrt{\eta_{02}^2-1}}{\eta_{02}^2} \qquad (2.18)$$

where η_{01}^2, η_{02}^2 are the squares of the refractive index for their respective media and are given by,

$$\eta_{01}^2 = \frac{\epsilon_1}{\epsilon_0} - j\frac{\sigma_1}{\omega\epsilon_0} \qquad (2.19)$$

$$\eta_{02}^2 = \frac{\epsilon_2}{\epsilon_0} - j\frac{\sigma_2}{\omega\epsilon_0}\,. \qquad (2.20)$$

The $F_1(\cdot)$ and $F_2(\cdot)$ functions are the Sommerfeld attenuation functions [25] for propagation over the iceberg and ocean surface media, respectively. The attenuation function for the iceberg medium is shown below in (2.21). The same form applies for $F_2(\cdot)$, except the "1" subscripts are replaced by "2" subscripts.

$$F_1(\rho) = 1 - j\sqrt{\pi p_1}\, e^{-p_1} \operatorname{erfc}(j\sqrt{p_1}) \tag{2.21}$$

where p_1 is the numerical distance given by

$$p_1 = -jk\frac{\Delta_1^2}{2}\rho\,. \tag{2.22}$$

In (2.21), the function, erfc$(\cdot)$, is the complementary error function (see, for example, [26]).

Recalling the definition of the Heaviside function h_R from (2.1), it is clear that $h_R E_z^{z+}$ in (2.15) represents the electric field within the iceberg region R (see Figure 2.1) while $(1 - h_R)E_z^{z+}$ in (2.16) is the electric field outside of the iceberg region. The electric field will be observed by the receive antenna at a location outside of the iceberg. As a result, the $(1 - h_R)E_z^{z+}$ term is the quantity of interest for this analysis and the $h_R E_z^{z+}$ need not be considered.

Comparing the functional form of (2.16) with Equations (51)-(54) of Walsh and Gill [21], Equation (2.16) may be grouped as follows,

$$E_z^{z+} = \left(E_z^{z+}\right)_0 + \left(E_z^{z+}\right)_1 + \left(E_z^{z+}\right)_2 \tag{2.23}$$

where

$$\left(E_z^{z+}\right)_0 = \frac{I\Delta\ell k^2}{j\omega\epsilon_0(2\pi)} \cdot F_2(\rho_0)\frac{e^{-jk\rho_0}}{\rho_0} \tag{2.24}$$

$$\left(E_z^{z+}\right)_1 = \frac{I\Delta\ell k^2}{j\omega\epsilon_0(2\pi)}\frac{jk(\Delta_2-\Delta_1)}{2\pi}\left[F_2(\rho)\frac{e^{-jk\rho}}{\rho}\overset{xy}{*}h_R\cdot F_2(\rho_0)\frac{e^{-jk\rho_0}}{\rho_0}\right] \tag{2.25}$$

$$\begin{aligned}\left(E_z^{z+}\right)_2 = {} & \frac{I\Delta\ell k^2}{j\omega\epsilon_0(2\pi)}\frac{jk(\Delta_2-\Delta_1)}{2\pi}\cdot F_2(\rho)\frac{e^{-jk\rho}}{\rho}\\ & \overset{xy}{*}h_R\left\{\frac{jk(\Delta_2-\Delta_1)}{2\pi}\left[F_1(\rho)\frac{e^{-jk\rho}}{\rho}\overset{xy}{*}h_R\cdot F_2(\rho_0)\frac{e^{-jk\rho_0}}{\rho_0}\right]\right\}.\end{aligned} \tag{2.26}$$

In the above equations the $(1-h_R)$ term has been suppressed with understanding that the equations hold only for (x,y) outside of the iceberg region. It should first be noted that the $(E_z^{z+})_0$ term is simply the equation for propagation over a smooth plane surface, i.e. the field due to the source. This term does not contribute to the field backscattered from the iceberg. Since an expression for the backscattered electric field is required, only the $(E_z^{z+})_1$ and $(E_z^{z+})_2$ terms are analyzed here. In the following section the physical significance of these two terms is investigated. It is found that the $(E_z^{z+})_1$ term represents single scattering off the iceberg region while $(E_z^{z+})_2$ accounts for double scattering within the iceberg region.

2.4 Physical Interpretation of $(E_z^{z+})_1$ and $(E_z^{z+})_2$

The two electric field terms, $(E_z^{z+})_1$ and $(E_z^{z+})_2$, given by equations (2.25) and (2.26), are referred to as the “first-order” and “second-order” field equations, respectively. For convenience, let the common terms in front of the convolutions in (2.25) and (2.26) be represented by a placeholder variable, D,

$$D = \frac{I\Delta\ell k^2}{j\omega\epsilon_0(2\pi)}\frac{jk(\Delta_2-\Delta_1)}{2\pi}\,. \tag{2.27}$$

Using (2.27) in (2.25) and (2.26) results in the following expressions for the first and second-order fields,

$$\left(E_z^{z+}\right)_1 = D\left[F_2(\rho)\frac{e^{-jk\rho}}{\rho} \overset{xy}{*} h_R \cdot F_2(\rho_0)\frac{e^{-jk\rho_0}}{\rho_0}\right] \tag{2.28}$$

$$\begin{aligned}\left(E_z^{z+}\right)_2 = D \cdot F_2(\rho)\frac{e^{-jk\rho}}{\rho} \overset{xy}{*} h_R &\left\{\frac{jk(\Delta_2-\Delta_1)}{2\pi}\right.\\ &\left.\cdot\left[F_1(\rho)\frac{e^{-jk\rho}}{\rho} \overset{xy}{*} h_R \cdot F_2(\rho_0)\frac{e^{-jk\rho_0}}{\rho_0}\right]\right\}\end{aligned} \tag{2.29}$$

where the two-dimensional spatial convolution, $\overset{xy}{*}$, has its typical definition of

$$f(x,y) \overset{xy}{*} g(x,y) = \int_{-\infty}^{\infty}\int_{-\infty}^{\infty} f(x-x', y-y')\, g(x',y')\, dx'\, dy'\,. \tag{2.30}$$

2.4.1 First-order Field Equation

The physical significance of the first-order field equation will be assessed first. Referring to the convolution definition given by (2.30) let $f(x,y) = F_2(\rho)\frac{e^{-jk\rho}}{\rho}$ and $g(x,y) = h_R \cdot F_2(\rho_0)\frac{e^{-jk\rho_0}}{\rho_0}$. Now, the convolution in (2.28) may be explicitly written as

$$\begin{aligned}\left(E_z^{z+}\right)_1 &= D\int_{-\infty}^{\infty}\int_{-\infty}^{\infty} F_2(\rho_c)\frac{e^{-jk\rho_c}}{\rho_c}\cdot h_R(x',y')F_2(\rho_0')\frac{e^{-jk\rho_0'}}{\rho_0'}\, dx'\, dy'\\ &= D\iint\limits_R F_2(\rho_c)F_2(\rho_0')\frac{e^{-jk(\rho_c+\rho_0')}}{\rho_c\rho_0'}\, dx'\, dy'\end{aligned} \tag{2.31}$$

where

$$\rho_c = \sqrt{(x - x')^2 + (y - y')^2}$$
$$\rho_0' = \sqrt{(x_0 + x')^2 + (y')^2}$$

and the double integral in (2.31) is over all points (x', y') in R.

In order to interpret the physical meaning of the first-order field, the geometry of (2.31) must be determined. To this end, the distance variables ρ_c and ρ_0' can be plotted, resulting in the scattering geometry depicted in Figure 2.2.

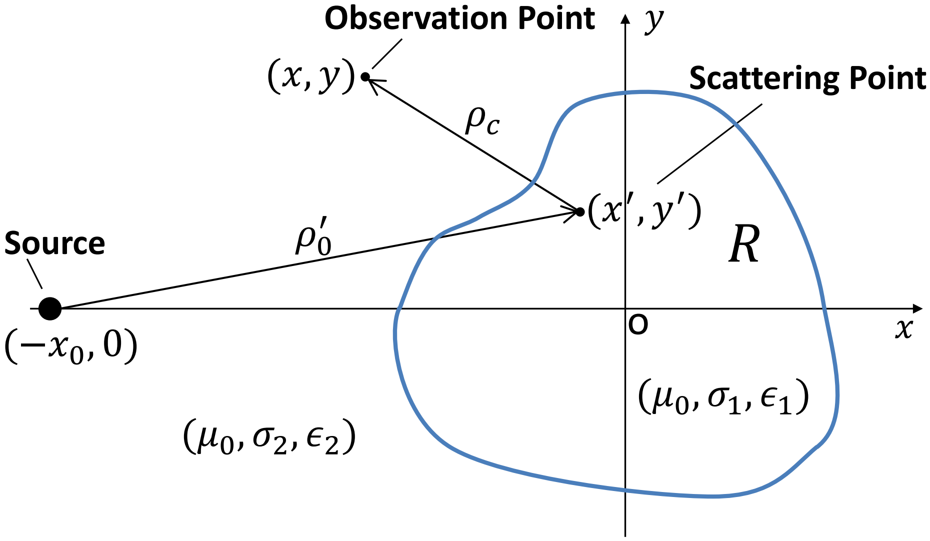

Figure 2.2: First-order scattering geometry

From the figure it is clear that ρ_0' represents the distance from the transmit antenna to a point in the iceberg region. This point is labeled as the scattering point and has coordinates (x', y'). The variable ρ_c is the distance from the scattering point to some observation point located at (x, y). This observation point corresponds to the physical location of the receive antenna. Observing the field at this point is equivalent to evaluating the expression given by (2.31) at coordinates (x, y).

Recall that $F_2(\cdot)$ is the Sommerfeld attenuation function for the ocean medium. As indicated in (2.21), $F_2(\cdot)$ is a function of distance. For a distance variable ρ, $F_2(\rho)$ gives the total attenuation of the electric field as it traverses a distance ρ over the ocean surface [27]. The first-order field equation, (2.31), contains two of these attenuation functions. One is a function of the distance variable ρ_c and the other a function of ρ'_0. $F_2(\rho'_0)$ represents the attenuation of the transmitted radiation as it travels from the transmit antenna to the scattering point (x', y'), in the iceberg region. Similarly $F_2(\rho_c)$ represents the attenuation of the radiation as it travels from the scattering point to the observation point at (x, y). Since the field expression only accounts for attenuation over the distances ρ'_0 and ρ_c, this suggests that (2.31) represents a single scatter of the transmitted signal off the iceberg. The transmitted radiation reflects off a point in the iceberg region and a portion of this then travels to the observation point. This type of scattering is referred to as "first-order" electromagnetic scattering [21].

Figure 2.2 shows only the contribution to the electric field at the observation point resulting from one point, (x', y'). As mentioned earlier, the double integral in (2.31) is over all points (x', y') in R. This implies that the total field observed at (x, y) is due to first-order scatters off every point in the iceberg region.

It is worth noting that equation (2.31) appears to only account for attenuation over the ocean surface, since the Sommerfeld attenuation terms $F_2(\rho_c)$, $F_2(\rho'_0)$ have subscripts "2" and therefore are for attenuation over the ocean surface. However, in Figure 2.2, it is clear that a small portion of the path for both distances ρ'_0, ρ_c is contained in the iceberg region. One would expected that a $F_1(\cdot)$ term should be present to account for this medium change. This issue is addressed in Section 2.4.3.

2.4.2 Second-order Field Equation

The second-order electric field equation, (2.29), can be interpreted in a similar manner to the first-order field equation. Applying the definition of the two-dimensional convolution $\overset{xy}{*}$ given by equation (2.30) to the outer convolution of the second-order equation results in

$$\begin{aligned}\left(E_z^{z+}\right)_2 = D \cdot \int_{-\infty}^{\infty}\int_{-\infty}^{\infty} F_2(\rho_c)\frac{e^{-jk\rho_c}}{\rho_c} \cdot h_R(x',y') \Bigg\{ \frac{jk(\Delta_2-\Delta_1)}{2\pi} \\ \cdot \left[F_1(\rho')\frac{e^{-jk\rho'}}{\rho'} \overset{xy}{*} h_R(x',y') \cdot F_2(\rho_0')\frac{e^{-jk\rho_0'}}{\rho_0'} \right] \Bigg\}\, dx'\, dy' \end{aligned} \tag{2.32}$$

where

$$\begin{aligned}\rho_c &= \sqrt{(x-x')^2+(y-y')^2} \\ \rho' &= \sqrt{(x')^2+(y')^2} \\ \rho_0' &= \sqrt{(x'+x_0)^2+(y')^2}\,.\end{aligned}$$

Now, carrying out the inner convolution and noting that the Heaviside function $h_R(x',y')$ is non-zero only for x', y' in R, equation (2.32) becomes

$$\begin{aligned}\left(E_z^{z+}\right)_2 = D \cdot \iint\limits_R F_2(\rho_c)\frac{e^{-jk\rho_c}}{\rho_c} \Bigg\{ \frac{jk(\Delta_2-\Delta_1)}{2\pi} \\ \cdot \left[\int_{-\infty}^{\infty}\int_{-\infty}^{\infty} F_1(\rho_a)\frac{e^{-jk\rho_a}}{\rho_a} \cdot h_R(x'',y'') F_2(\rho_0'')\frac{e^{-jk\rho_0''}}{\rho_0''}\, dx''\, dy'' \right] \Bigg\}\, dx'\, dy' \end{aligned} \tag{2.33}$$

where

$$\rho_a = \sqrt{(x' - x'')^2 + (y' - y'')^2}$$
$$\rho_0'' = \sqrt{(x'' + x_0)^2 + (y'')^2}\,.$$

Rearranging terms and applying the Heaviside function $h_R(x'', y'')$ gives the desired form of the second-order field equation as

$$\begin{aligned}\left(E_z^{z+}\right)_2 = D \cdot \iint\limits_R F_2(\rho_c)\frac{e^{-jk\rho_c}}{\rho_c} \Bigg\{ & \frac{jk(\Delta_2 - \Delta_1)}{2\pi} \\ & \cdot \iint\limits_R F_1(\rho_a)F_2(\rho_0'')\frac{e^{-jk(\rho_a+\rho_0'')}}{\rho_a\rho_0''}\,dx''\,dy'' \Bigg\}\,dx'\,dy'\,. \end{aligned} \tag{2.34}$$

The distance variables ρ_0'', ρ_a, and ρ_c in (2.34) provide insight into the scattering geometry of the second-order field. This geometry is shown in Figure 2.3. As suggested by the figure, the second-order field equation represents a double scatter within the iceberg region. This is reflected in the mathematics of (2.34). The outer double integral is over all (x', y') in the iceberg region. Furthermore, for each (x', y') the inner integral is over all (x'', y'') in the iceberg region.

Consider the contribution to the total second-order field observed at (x, y) due to scattering at a particular (x', y') and (x'', y''). As indicated in Figure 2.3, the transmitted radiation travels a distance ρ_0'' from the source to the first scattering point, (x'', y''). The attenuation over this distance is accounted for in (2.34) through the $F_2(\rho_0'')$ term. At (x'', y'') the transmitted signal scatters and the radiation travels another ρ_a to the point (x', y'). Recalling that $F_1(\cdot)$ represents the attenuation of a signal propagating over the iceberg medium, $F_1(\rho_a)$ in (2.34) accounts for the atten-

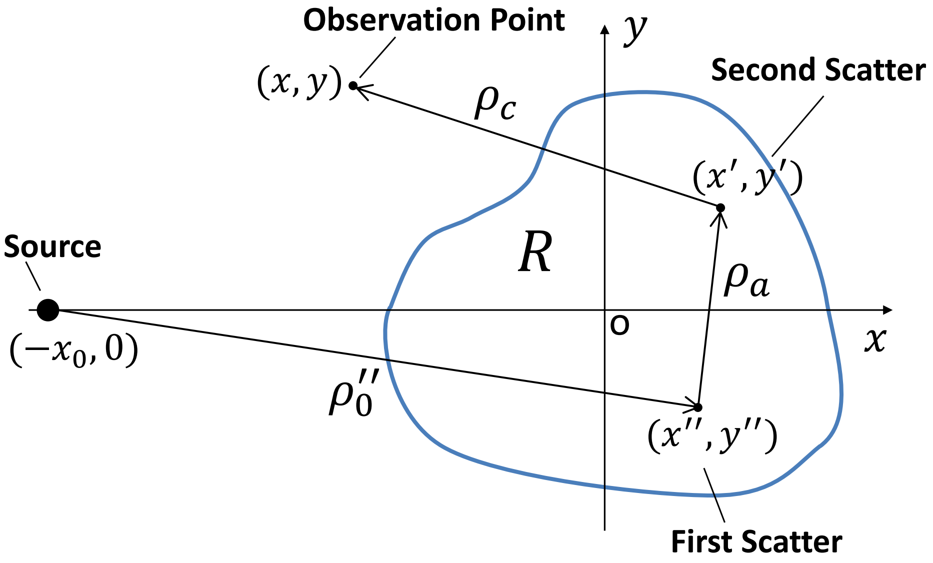

Figure 2.3: Second-order scattering geometry

uation over this distance. It is important to note that the presence of the iceberg medium attenuation function makes good sense from a physical perspective since ρ_a is completely contained in the iceberg region. Finally, the radiation is scattered at (x', y') and travels a distance ρ_c back to the observation point. This attenuation is accounted for in the outer integral of (2.34) by $F_2(\rho_c)$. As expected this is the function for attenuation over water. However, as was the case for the first-order field, a portion of the path for distances ρ_0'' and ρ_c is in the iceberg region. Yet there are no $F_1(\cdot)$ terms to account for these portions.

Thus for a fixed (x', y') and (x'', y'') equation (2.34) describes a double scatter within the iceberg region. This is referred to as second-order electromagnetic scattering [21]. Of course, the total second-order field at the observation point is due to double scattering off every point of the iceberg. For a fixed (x', y') the inner integral implies that the contribution to the total field at (x, y) is due to a double scatter involving every (x'', y'') in R with the fixed second scatter point of (x', y'). The outer integral of (2.34) repeats this process for every (x', y') in R. Equation (2.34) therefore describes the total field at the observation point due to a multitude of second-order scatters within the iceberg region.

2.4.3 Discussion of Sommerfeld Attenuation Functions in Electric Field Equations

It was noted in Section 2.4.1 and 2.4.2 that there are portions of the radar signal which traverse the iceberg region, yet there is no iceberg attenuation function $F_1(\cdot)$ in (2.31) and (2.34) to account for this. For the first-order field, both distances ρ_0', ρ_c have a portion of their path in the iceberg region (see Figure 2.2). Similarly for the second-order field, the distances ρ_0'', ρ_c have a portion of their path in the iceberg region (see Figure 2.3).

From a practical standpoint, the lack of the iceberg attenuation function is a reasonable approximation since the iceberg itself will be much smaller than the distance from the iceberg to both the source and observation points. As such, almost all the path of ρ_0', ρ_c, and ρ_0'' will be over the ocean surface. This, coupled with the fact that simulated results using these electric field equations were found to be in good agreement with field data in [19], supports the idea that both (2.31) and (2.34) are good approximations to the actual electric field.

Chapter 3

Backscattered Electric Field and Iceberg Radar Cross Section Derivation

The derivation of the backscattered electric field and iceberg RCS is presented in this chapter.

Starting in Section 3.1 the derivation deviates from Walsh's approach and the electric field equation is modified to account for a pulsed sinusoid excitation (Section 3.2). After obtaining the backscattered electric field at the receiver, a physical interpretation of this field equation is provided in Section 3.3 and compared with the physical interpretation offered previously in Section 2.4. In Section 3.4, the backscattered electric field is further simplified by assuming the iceberg under observation fits within a single radar patch width. Finally, the RCS equation for an iceberg is obtained and discussed in Section 3.5.

3.1 Time Domain Analysis of the Backscattered Electric Field

In Section 2.4 it was shown that the total electric field observed was due to contributions from both the first-order and second-order field expressions. It was further demonstrated that these expressions describe two different types of physical scattering phenomenon. In order to limit the scope of this thesis, the remainder of the derivation will assess only the first-order field equation. The second-order field expression will be the subject of future work.

3.1.1 Monostatic Radar Configuration

The equations for the first and second-order fields given by (2.31) and (2.34), respectively, involve minimal assumptions about the characteristics of the physical HFSWR system. For example, neither expression has assumed a specific location for the receive antenna nor the form of the waveform which will excite the transmit antenna. The general nature of (2.31) and (2.34) enables them to be applied to a variety of real world HFSWR systems.

In order to further simplify these general expressions, and obtain a practical expression for the backscattered electric field from an iceberg, some assumptions about the physical HFSWR system must be made. The first major assumption for this derivation is that the transmit and receive antennas are co-located. This is a very common setup for HFSWR systems and is known as a monostatic radar configuration.

Focusing now on the first-order electric field, equation (2.31) may be rewritten using (2.27) to give,

$$\begin{aligned}\left(E_z^{z+}\right)_1(x,y) =& \frac{I\Delta\ell k^2}{j\omega\epsilon_0(2\pi)}\frac{jk(\Delta_2-\Delta_1)}{2\pi}\\ &\cdot\iint\limits_R F_2(\rho_c)F_2(\rho_0')\frac{e^{-jk(\rho_c+\rho_0')}}{\rho_c\rho_0'}\,dx'\,dy' \end{aligned}\tag{3.1}$$

where it is recalled that,

$$\begin{aligned}\rho_c &= \sqrt{(x-x')^2+(y-y')^2}\\ \rho_0' &= \sqrt{(x_0+x')^2+(y')^2}\,.\end{aligned}$$

For a monostatic system the receive antenna will be located at the same coordinates as the transmit antenna. Here, these coordinates are $(x,y)=(-x_0,0)$. It may be recalled from Section 2.4.1 that observing the field at a point (x,y) is equivalent to evaluating the field at that point. Since the field will be observed at the receive antenna, equation (3.1) may be evaluated at $(x,y)=(-x_0,0)$ to give the backscattered field. Noting that this substitution implies $\rho_c=\rho_0'$ the backscattered electric field is now given by

$$\left[\left(E_z^{z+}\right)_1\right]_b = \frac{I\Delta\ell k^2}{j\omega\epsilon_0(2\pi)}\frac{jk(\Delta_2-\Delta_1)}{2\pi}\cdot\iint\limits_R\frac{F_2^2(\rho_0')}{(\rho_0')^2}e^{-2jk\rho_0'}\,dx'\,dy'\,. \tag{3.2}$$

The subscript b has been added to indicate that (3.2) refers to the backscattered electric field.

3.1.2 Time Domain Expression

The derivation of Equation (3.2) has been carried out completely in the Fourier transform domain and is therefore a function of radian frequency ω. Before specifying an excitation current waveform, Equation (3.2) is first brought to the time domain. In order to do this, an inverse Fourier transform $\mathcal{F}_t^{-1}(\ )$ is performed. Noting that multiplication in the frequency domain becomes a convolution in the time domain, Equation (3.2) may be written as

$$\begin{aligned}\left[\left(E_z^{z+}\right)_1\right]_b(t) =& \frac{1}{(2\pi)^2}\mathcal{F}_t^{-1}\left\{\frac{I\Delta\ell k^2\cdot jk}{j\omega\epsilon_0}\right\} \\ & \overset{t}{*}\,\mathcal{F}_t^{-1}\left\{(\Delta_2-\Delta_1)\iint\limits_R \frac{F_2^2(\rho_0')}{(\rho_0')^2}e^{-2jk\rho_0'}\,dx'\,dy'\right\}. \end{aligned} \tag{3.3}$$

Clearly, equation (3.3) contains two inverse Fourier transforms. The inverse transform involving the dipole current I will be considered first. Up to this point no assumptions have been made regarding the form of the current I and it is in general a function of ω. Recalling that $k=\omega/c$, where c is the speed of light, it is easily found that

$$\begin{aligned}\mathcal{F}_t^{-1}\left\{\frac{I\Delta\ell k^2\cdot jk}{j\omega\epsilon_0}\right\} &= \mathcal{F}_t^{-1}\left\{\frac{\eta_0\Delta\ell}{c^2}\omega^2 I(\omega)\right\} \\ &= -\frac{\eta_0\Delta\ell}{c^2}\mathcal{F}_t^{-1}\left\{(j\omega)^2 I(\omega)\right\} \end{aligned} \tag{3.4}$$

where $\eta_0=\sqrt{\mu_0/\epsilon_0}$ is the intrinsic impedance of free space and $c=\sqrt{1/(\mu_0\epsilon_0)}$. Recognizing that the inverse Fourier transform of a function multiplied by $(j\omega)^2$ gives the second derivative of the function (3.4) becomes

$$\mathcal{F}_t^{-1}\left\{\frac{I\Delta\ell k^2\cdot jk}{j\omega\epsilon_0}\right\} = -\frac{\eta_0\Delta\ell}{c^2}\frac{\partial^2 i(t)}{\partial t^2} \tag{3.5}$$

where $i(t)$ is the time domain current expression.

Next, the second inverse transform of (3.3) is considered, i.e.

$$\mathcal{F}_t^{-1}\left\{(\Delta_2-\Delta_1)\iint\limits_R \frac{F_2^2(\rho_0')}{(\rho_0')^2}e^{-2jk\rho_0'}\,dx'\,dy'\right\}\,. \tag{3.6}$$

It should be noted that both $F_2(\cdot)$ and $(\Delta_2-\Delta_1)$ are functions of the transform variable ω, and hence enter the inverse transform process. However, these two terms can be shown to be approximately constant over the frequency band of interest. Following the approach in [21] and [22] the Sommerfeld attenuation term $F_2(\omega,\rho_0')$ may approximated by $F_2(\omega_0,\rho_0')$ where ω_0 is the dominant frequency of the source excitation current. Similarly the $(\Delta_2-\Delta_1)$ term may also be evaluated at $\omega=\omega_0$ since it varies very slowly over the frequency band of interest. Simulations of this term for a typical HFSWR operating frequency of $f_0=13.5$ MHz and bandwidth of 100 kHz show its magnitude varies between 0.272515 to 0.273174 over the frequency band. This also holds for other frequencies in the high-frequency band. For example at operating frequency $f_0=25.4$ MHz and bandwidth 100 kHz, $(\Delta_2-\Delta_1)$ varies between 0.318076 and 0.318275. As a result, this term is also considered constant with respect to frequency and (3.6) becomes

$$\begin{aligned}\mathcal{F}_t^{-1}&\left\{(\Delta_2-\Delta_1)\iint\limits_R \frac{F_2^2(\rho_0')}{(\rho_0')^2}e^{-2jk\rho_0'}\,dx'\,dy'\right\}\\ &\approx(\Delta_2-\Delta_1)\iint\limits_R \frac{F_2^2(\rho_0')}{(\rho_0')^2}\mathcal{F}_t^{-1}\left\{e^{-2jk\rho_0'}\right\}\,dx'\,dy'\\ &=(\Delta_2-\Delta_1)\iint\limits_R \frac{F_2^2(\rho_0')}{(\rho_0')^2}\delta\left(t-\frac{2\rho_0'}{c}\right)\,dx'\,dy'\,.\end{aligned} \tag{3.7}$$

Now, using equations (3.5) and (3.7) in (3.3) the backscattered electric field may be written as

$$\begin{aligned}\left[\left(E_z^{z+}\right)_1\right]_b(t) = &-\frac{\eta_0 \Delta \ell}{c^2 (2\pi)^2}(\Delta_2 - \Delta_1) \\ &\cdot \frac{\partial^2 i(t)}{\partial t^2} \overset{t}{*} \iint\limits_R \frac{F_2^2(\rho_0')}{(\rho_0')^2} \delta\left(t - \frac{2\rho_0'}{c}\right) dx'\, dy' \,. \end{aligned} \tag{3.8}$$

3.2 Incorporating a Pulsed Source

The expression given by (3.8) represents the first-order backscattered electric field from an iceberg for a vertical dipole source with general current excitation $i(t)$. This excitation current could take any form depending on the required application. In this analysis, a pulsed current excitation is assumed. This could easily be replaced with an FMCW or FMICW (frequency modulated interrupted continuous wave) waveform if desired.

Referring to [21] the expression for the current waveform for the pulsed case is given by

$$i(t) = I_0 e^{j\omega_0 t} \cdot \left\{ h\left[t + \frac{T_r}{2}\right] - h\left[t - \frac{T_r}{2}\right] \right\} \tag{3.9}$$

where ω_0 is the radian operating frequency, T_r is the transmitted pulse width, and I_0 is the peak current amplitude. Here, $h(\cdot)$ again represents the Heaviside function. An example of a pulsed waveform is shown in Figure 3.1. If the leading and trailing edge terms are ignored as they are in [21] the second time derivative of (3.9) may be approximated as

$$\frac{\partial^2 i(t)}{\partial t^2} \approx -\omega_0^2 I_0 e^{j\omega_0 t} \cdot \left\{ h\left[t + \frac{T_r}{2}\right] - h\left[t - \frac{T_r}{2}\right] \right\} \,. \tag{3.10}$$

Substituting (3.10) into (3.8) gives

$$\begin{aligned}\left[\left(E_z^{z+}\right)_1\right]_b(t) =& \frac{I_0\eta_0\Delta\ell k_0^2}{(2\pi)^2}(\Delta_2-\Delta_1)\cdot\left[e^{j\omega_0 t}\left\{h\left[t+\frac{T_r}{2}\right]-h\left[t-\frac{T_r}{2}\right]\right\}\right]\\ &\overset{t}{*}\left[\iint\limits_R \frac{F_2^2(\rho_0')}{(\rho_0')^2}\delta\left(t-\frac{2\rho_0'}{c}\right)dx'\,dy'\right]\end{aligned} \tag{3.11}$$

where $k_0 = \omega_0/c$.

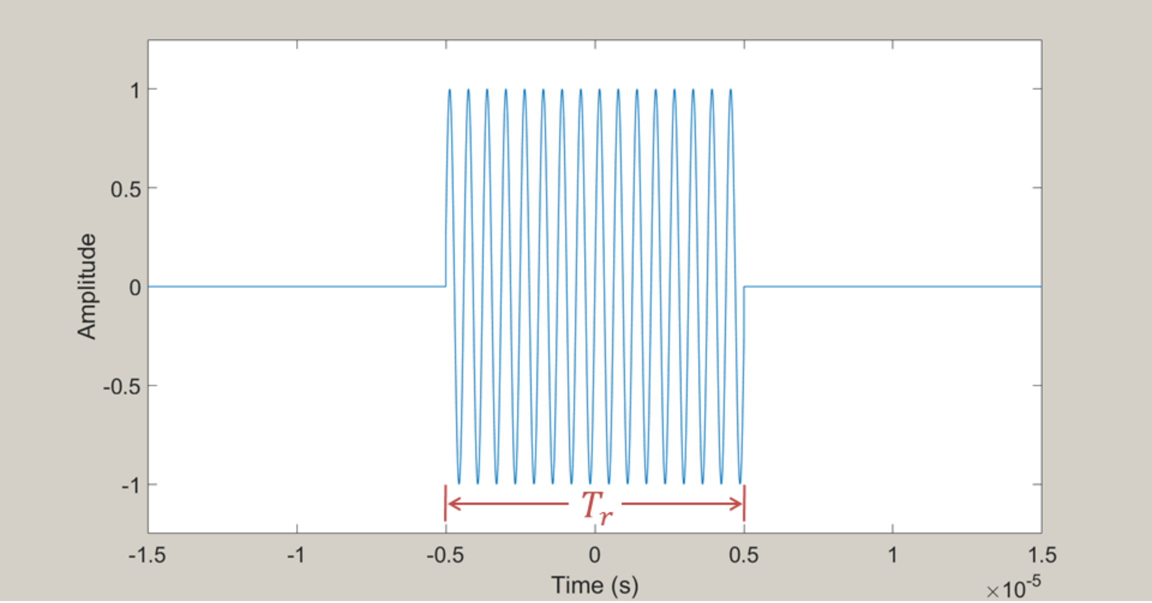

Figure 3.1: Example of pulsed sinusoidal waveform

The double integral in (3.11) is over the spatial coordinates x', y'. As noted in Section 2.4.1 and depicted again in the Figure 3.2, ρ_0' is the radial distance from the radar antenna to a point in the iceberg region. A coordinate transform may be performed on the double integral to express it in terms of radial distance and angle relative to the antenna. This transformation first involves a linear shift of the origin from $(0, 0)$ to $(-x_0, 0)$. Next the coordinate system is converted to the polar coordinates (ρ_0', ϕ). The result of this transform is

$$\iint\limits_R \frac{F_2^2(\rho_0')}{(\rho_0')^2}\delta\left(t - \frac{2\rho_0'}{c}\right) dx'\, dy' = \int_\phi \int_{\rho_1(\phi)}^{\rho_2(\phi)} \frac{F_2^2(\rho_0')}{\rho_0'}\delta\left(t - \frac{2\rho_0'}{c}\right) d\rho_0'\, d\phi \qquad (3.12)$$

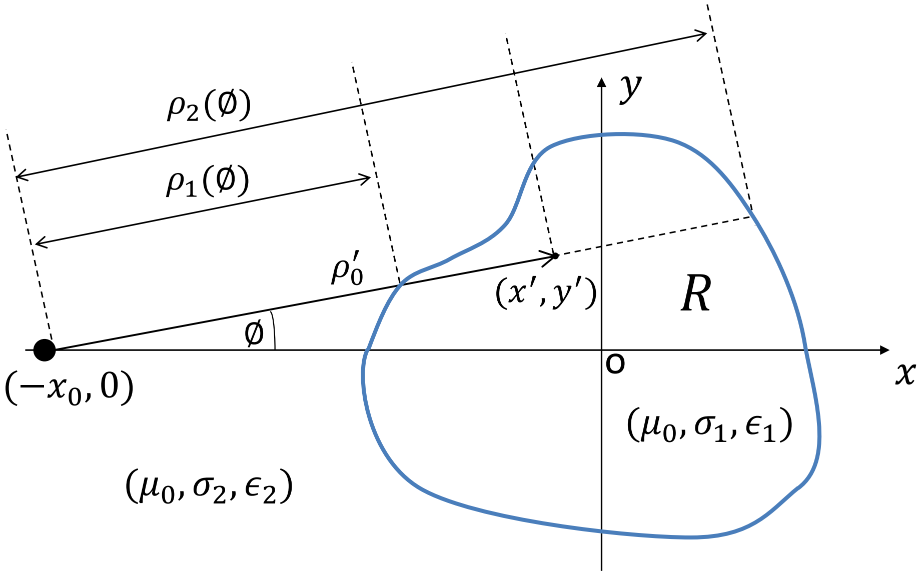

Figure 3.2: Scatter geometry (top view)

where $\rho_2(\phi)$ and $\rho_1(\phi)$ are, respectively, the upper and lower limits on the distance variable ρ_0' for a given ϕ. This is shown in Figure 3.2. The $d\phi$ integral in (3.12) is over all angular rays which intersect the region R.

Equation (3.12) may now be substituted into (3.11) to give,

$$\begin{aligned}\left[\left(E_z^{z+}\right)_1\right]_b(t) = &\frac{I_0\eta_0\Delta\ell k_0^2}{(2\pi)^2}(\Delta_2 - \Delta_1)\cdot\left[e^{j\omega_0 t}\left\{h\left[t + \frac{T_r}{2}\right] - h\left[t - \frac{T_r}{2}\right]\right\}\right] \\ &\overset{t}{*}\left[\int_\phi \int_{\rho_1(\phi)}^{\rho_2(\phi)} \frac{F_2^2(\rho_0')}{\rho_0'}\delta\left(t - \frac{2\rho_0'}{c}\right) d\rho_0'\, d\phi\right]. \qquad (3.13)\end{aligned}$$

This equation can be further simplified by evaluating the time convolution. The convolution involves a delta function which produces a shift of $2\rho_0'/c$ in the time variable. Carrying out this convolution, (3.13) becomes,

$$\left[\left(E_z^{z+}\right)_1\right]_b(t) = \frac{I_0\eta_0\Delta\ell k_0^2}{(2\pi)^2}(\Delta_2-\Delta_1)\cdot e^{j\omega_0 t}\int_\phi\int_{\rho_1(\phi)}^{\rho_2(\phi)}\frac{F_2^2(\rho_0')}{\rho_0'}e^{-2jk_0\rho_0'} \cdot\left\{h\left[t-\frac{2\rho_0'}{c}+\frac{T_r}{2}\right]-h\left[t-\frac{2\rho_0'}{c}-\frac{T_r}{2}\right]\right\}d\rho_0'\,d\phi\,. \qquad (3.14)$$

This is the first-order equation for the field backscattered from an iceberg.

3.3 Physical Interpretation of the Backscattered Electric Field

In Section 2.4.1, the physical significance of Walsh's general first-order electric field expression was analyzed. It was found that the field observed at a location (x, y) is the result of first-order scattering off every point in the iceberg region. With the assumptions that the HFSWR system under investigation is a monostatic radar system driven by a pulsed sinusoid current waveform, Walsh's original frequency domain expression in (2.31) has since been reduced to the time-domain equation of (3.14). A brief interpretation of (3.14) shows that the conclusions drawn in Section 2.4.1 are still valid for this simplified field equation.

The field in Section 2.4.1 was shown to propagate a distance ρ_0' to the iceberg, scatter, then travel another ρ_c to the observation point. This was represented by the $F_2(\rho_c)\cdot F_2(\rho_0')$ attenuation term in equation (2.31). With the observation point now at the same location as the transmit antenna, ρ_c becomes equal to ρ_0'. This is reflected in (3.14) by the replacement of $F_2(\rho_c)\cdot F_2(\rho_0')$ with the attenuation term $F_2^2(\rho_0')$ which represents attenuation over a distance of $2\rho_0'$. Furthermore, as in equation (2.31), the double integral in (3.14) is also over all points in the iceberg region. Thus, the total received field described by (3.14) is also due to single scatters off each point in the iceberg region.

The above arguments use the attenuation function $F_2(\cdot)$ to reason the physical scattering mechanisms described by the field equations. Now that the backscattered field is in the time domain, the idea that (3.14) only describes single scattering can be verified from another perspective. This may be completed by assessing the times, t, for which the backscattered field exists. The Heaviside functions in the double integral of (3.14) restrict the field to be non-zero only during the time interval

$$\left(\frac{2\rho_0'}{c} - \frac{T_r}{2}\right) < t < \left(\frac{2\rho_0'}{c} + \frac{T_r}{2}\right) .$$

Of course ρ_0' will take on a range of values which is determined by the iceberg's shape. There will however, exist some minimum distance ρ_{min} corresponding to the closest part of the iceberg and some maximum distance ρ_{max} corresponding to the most distant part of the iceberg. The double integral will include all ρ_0' between these values so the backscattered field of (3.14) will be non-zero for the time interval

$$\left(\frac{2\rho_{\text{min}}}{c} - \frac{T_r}{2}\right) < t < \left(\frac{2\rho_{\text{max}}}{c} + \frac{T_r}{2}\right) . \tag{3.15}$$

Referring to the excitation current expression given by (3.9) it may be seen that the transmitted signal begins at time $t = -T_r/2$. After traveling a distance ρ_{min} to the closest point on the iceberg the signal scatters once and travels another ρ_{min} to the receiver. Given that the radiated signal moves with speed c the time taken to travel this distance is $2\rho_{\text{min}}/c$ and the backscattered field first is observed at

$$t_{\text{min}} = \frac{2\rho_{\text{min}}}{c} - \frac{T_r}{2} \,. \tag{3.16}$$

The transmitted pulse ends at time $t = +T_r/2$, so the scatter from this portion of the transmitted signal off the farthest point of the iceberg is not received till $2\rho_{\text{max}}/c$ seconds later. Therefore, the backscattered field ends at time

$$t_{\text{max}} = \frac{2\rho_{\text{max}}}{c} + \frac{T_r}{2} \,. \tag{3.17}$$

If Equation (3.14) were to represent any higher scattering orders, the received field would have to exist at times greater than t_{max}. This is because if multiple scatters within the iceberg region occurred it would be possible for the total distance travelled by the signal to be greater than $2\rho_{\text{max}}$ leading to (3.14) being non-zero for $t > t_{\text{max}}$. However, as shown in (3.15), this is not the case and thus further supports the fact that (3.14) describes the electric field which is due to first-order scattering only.

3.4 Backscattered Field Simplification

Equation (3.14) describes the first-order backscattered field for an iceberg of arbitrary shape and size. With an aim of reducing (3.14) to a more tractable form, consider the distance $\rho_0' = x_0$. Referring to Figure 3.2 this distance is the distance to the center of the iceberg region. The time $t_0 = 2x_0/c$ is then the amount of time for the transmitted signal to travel to the iceberg center and return. If the electric field is observed at time t_0, (3.14) becomes

$$\begin{aligned}\left[\left(E_z^{z+}\right)_1\right]_b(t_0) = \frac{I_0\eta_0\Delta\ell k_0^2}{(2\pi)^2}(\Delta_2-\Delta_1)\cdot e^{j\omega_0 t_0}\int_\phi\int_{\rho_1(\phi)}^{\rho_2(\phi)}\frac{F_2^2(\rho_0')}{\rho_0'}e^{-2jk_0\rho_0'} \\ \cdot\left\{h\left[\frac{2}{c}\left(x_0+\frac{cT_r}{4}-\rho_0'\right)\right]-h\left[\frac{2}{c}\left(x_0-\frac{cT_r}{4}-\rho_0'\right)\right]\right\}\,d\rho_0'\,d\phi\,.\end{aligned} \tag{3.18}$$

The Heaviside functions in (3.18) then restrict the range of values ρ_0' may take on to

$$\left(x_0-\frac{cT_r}{4}\right)<\rho_0'<\left(x_0+\frac{cT_r}{4}\right)\,. \tag{3.19}$$

For any value of ρ_0' outside of this range the integral in (3.18) is zero. Hence, only distances in the above range contribute to the received field at time t_0. Thus, at any given time the radar can only "see" a depth of $cT_r/2$. This is commonly referred to as the "patch width" of the pulsed radar signal.

It is now assumed that the closest and furthest points of the iceberg (ρ_{min} and ρ_{max}) satisfy the following relationship,

$$\left(\rho_{\text{max}}-\rho_{\text{min}}\right)<cT_r/2\,.$$

This means that the entire iceberg is contained within one radar patch width. For a typical pulse width of 10 μs, $cT_r/2 = 1500$ m, so icebergs with radial widths up to 1500 m may be observed. This assumption implies that $\rho_{\text{min}} < \rho_0' < \rho_{\text{max}}$ is contained within the range given by (3.19), i.e.

$$\left(x_0-\frac{cT_r}{4}\right)<\rho_{\text{min}}<\rho_0'<\rho_{\text{max}}<\left(x_0+\frac{cT_r}{4}\right)\,.$$

As a result, the Heaviside functions in (3.18) equate to unity over the integration range resulting in,

$$\left[\left(E_z^{z+}\right)_1\right]_b(t_0) = \frac{I_0\eta_0\Delta\ell k_0^2}{(2\pi)^2}(\Delta_2-\Delta_1)\cdot e^{j\omega_0 t_0}\int_\phi\int_{\rho_1(\phi)}^{\rho_2(\phi)}\frac{F_2^2(\rho_0')}{\rho_0'}e^{-2jk_0\rho_0'}\,d\rho_0'\,d\phi \quad (3.20)$$

The $F_2^2(\rho_0')/\rho_0'$ term may be considered approximately constant over the integration range by applying the same assumption used in [21], since for normal operation $x_0 \gg cT_r/2$. After evaluating this term at $\rho_0' = x_0$, (3.18) may be written as

$$\left[\left(E_z^{z+}\right)_1\right]_b(t_0) \approx \frac{I_0\eta_0\Delta\ell k_0^2}{(2\pi)^2}(\Delta_2-\Delta_1)\cdot e^{j\omega_0 t_0}\frac{F_2^2(x_0)}{x_0}\int_\phi\int_{\rho_1(\phi)}^{\rho_2(\phi)}e^{-2jk_0\rho_0'}\,d\rho_0'\,d\phi\,. \quad (3.21)$$

Carrying out the ρ_0' integral in (3.21) the final form of the backscattered field is obtained as

$$\begin{aligned}\left[\left(E_z^{z+}\right)_1\right]_b(t_0) \approx{}& \frac{I_0\eta_0\Delta\ell k_0}{(2\pi)^2}(\Delta_2-\Delta_1)\cdot e^{j\omega_0 t_0}\frac{F_2^2(x_0)}{x_0}\\ &\cdot\int_\phi e^{-jk_0[\rho_2+\rho_1]}\sin\left[k_0(\rho_2-\rho_1)\right]\,d\phi \qquad (3.22)\end{aligned}$$

where the function notation has been dropped for the ρ_1, ρ_2 terms with understanding that they are both functions of ϕ.

3.5 Iceberg Radar Cross Section Derivation

With the final backscattered electric field in place, it is now possible to obtain an expression for the iceberg RCS. As briefly discussed in Chapter 1, the RCS is a representation of what the iceberg region looks like to a HFSWR. More specifically, the RCS is a measure of the iceberg's ability to reflect radar signals towards the radar receiver. The iceberg RCS will depend on several iceberg parameters including it's size and shape, as well as the electrical parameters (μ, σ, ϵ) of both the ice and the surrounding sea water. Once the RCS has been obtained, the expected received signal strength can be investigated as a function of these parameters.

3.5.1 Radar Range Equation

Obtaining the RCS for the iceberg region first involves finding the power, P_r, received by the radar. In general, the received power for a radar system is described by the radar range equation. This equation is dependent on the type of radar transmitter used, the distance to the target, the target's RCS, as well as several other parameters. For the radar system considered here the monostatic radar range equation is given by (see, for example, Barton [28]),

$$P_r = \left(\frac{\lambda_0^2 G_r P_t G_t |F_2(x_0)|^4}{(4\pi)^3 x_0^4} \right) \sigma \tag{3.23}$$

where σ is the RCS for the target under consideration, which in this case is the iceberg region. λ_0 is the wavelength of the transmitted signal and is given by $\lambda_0 = c2\pi/\omega_0$, P_t is the transmit power, and G_t, G_r are the transmitter and receiver gain, respectively. For an elementary vertical dipole antenna the product of the transmit power and gain, $P_t G_t$, may be expressed as (see [21]),

$$P_t G_t = \frac{\eta_0 k_0^2}{8\pi} \left| I_0 \Delta \ell \right|^2 . \tag{3.24}$$

It should also be noted that (3.23) has been evaluated at the distance x_0 which corresponds to the iceberg region's center.

With the radar range equation for this system in place, attention is now focused on finding the received power using the expression derived for the backscattered electric field, (3.22). By comparing the received power calculated using (3.22) against the standard radar range equation of (3.23) an expression for the RCS, σ, may be found.

3.5.2 Radar Cross Section

The power, P_r, received by an antenna located at $(x, y) = (-x_0, 0)$ may be estimated as in [18] and [21] using,

$$P_r = \frac{A_r \left| \left[(E_z^{z+})_1 \right]_b (t_0) \right|^2}{(2\eta_0)} \tag{3.25}$$

where A_r is the effective aperture of the receive antenna and is defined as

$$A_r = \frac{\lambda_0^2 G_r}{4\pi} \,. \tag{3.26}$$

Equation (3.22) is now rewritten for convenience as

$$\left[\left(E_z^{z+} \right)_1 \right]_b (t_0) \approx \frac{I_0 \eta_0 \Delta\ell k_0}{(2\pi)^2} (\Delta_2 - \Delta_1) \cdot e^{j\omega_0 t_0} \frac{F_2^2(x_0)}{x_0} \cdot g(\phi) \tag{3.27}$$

where $g(\phi)$ is

$$g(\phi) = \int_\phi e^{-jk_0[\rho_2 + \rho_1]} \sin\left[k_0(\rho_2 - \rho_1) \right] \, d\phi \,. \tag{3.28}$$

Using (3.27) in (3.25) gives

$$P_r = \frac{A_r}{2\eta_0} \frac{|I_0 \eta_0 \Delta\ell k_0|^2}{(2\pi)^4} \frac{|F_2^2(x_0)|^2}{x_0^2} \cdot \left| (\Delta_2 - \Delta_1) \cdot g(\phi) \right|^2 \,. \tag{3.29}$$

Substituting A_r in (3.29) with equation (3.26) results in

$$P_r = \frac{\lambda_0^2 G_r}{8\pi} \frac{\eta_0 k_0^2 |I_0 \Delta\ell|^2}{(2\pi)^4} \frac{|F_2(x_0)|^4}{x_0^2} \cdot \left|(\Delta_2 - \Delta_1) \cdot g(\phi)\right|^2 . \tag{3.30}$$

Recalling the expression for $P_t G_t$ from (3.24) and substituting this into (3.30) gives the received power expression as

$$P_r = \frac{\lambda_0^2 G_r P_t G_t |F_2(x_0)|^4}{(2\pi)^4 x_0^2} \cdot \left|(\Delta_2 - \Delta_1) \cdot g(\phi)\right|^2 . \tag{3.31}$$

This expression can now be placed into the same form as the radar range equation; i.e.,

$$P_r = \left(\frac{\lambda_0^2 G_r P_t G_t |F_2(x_0)|^4}{(4\pi)^3 x_0^4} \right) \cdot \left(\frac{4x_0^2}{\pi} \left|(\Delta_2 - \Delta_1) \cdot g(\phi)\right|^2 \right) . \tag{3.32}$$

Comparing (3.32) against the radar range equation of (3.23) and substituting $g(\phi)$ back in results in the RCS for the iceberg region:

$$\sigma = \frac{4x_0^2}{\pi} \left| (\Delta_2 - \Delta_1) \int_\phi e^{-jk_0[\rho_2 + \rho_1]} \sin\left[k_0(\rho_2 - \rho_1)\right] \, d\phi \right|^2 . \tag{3.33}$$

3.5.2.1 Analysis of the Iceberg RCS Equation

As discussed in Section 3.5, the RCS for an iceberg is a measure of an iceberg's ability to reflect signals back towards the radar receiver. After finding the final backscattered electric field equation for a pulsed sinusoid HFSWR system, the RCS for an arbitrarily shaped iceberg has been obtained and is described by equation (3.33). As expected and discussed below, (3.33) depends almost exclusively on the the iceberg's geometry, the electrical parameters of both the iceberg and the surrounding ocean, and the operating parameters of the HFSWR system.

Most notably, the iceberg's geometry is accounted for in (3.33) by the integral over ϕ. This integral is over the entire iceberg region and accounts for the shape of the iceberg through the distance variables ρ_1, ρ_2 which, respectively, correspond to the closest and farthest points of the iceberg for a given ϕ. Furthermore, the integral in (3.33) does not include any points within the iceberg. This is in contrast to the initial first-order electric field expression (2.31) which was discussed in Section 2.4.1. That expression involved a double integral over every point contained in the iceberg region. Here, the RCS depends only on the edges of the iceberg which are described by ρ_1, ρ_2. This is an important distinction as the final RCS expression only involves scattering off the iceberg's edges. This makes good physical sense as long as the iceberg has homogenous electrical properties.

The dependence of the RCS magnitude on the electrical parameters of the iceberg as well as the ocean surface are accounted for by the surface impedance terms $(\Delta_2 - \Delta_1)$ in (3.33).

Finally, (3.33) also involves two of the HFSWR's operating parameters. These parameters are the radar's operating frequency and the pulse width of the radar's transmit waveform. The operating frequency dependency arises primarily through the k_0 term which appears multiple times in (3.33), since $k_0 = \omega_0/c$ and ω_0 is the radian operating frequency. There is also a dependence on operating frequency through the surface impedance term $(\Delta_2 - \Delta_1)$. The pulse width, T_r, of the transmit waveform does not explicitly appear in the iceberg RCS equation. However, it was assumed in Section 3.4 that the observed iceberg is contained within one radar patch width. The patch width, which is given by $cT_r/2$, is in turn dependent on the radar's pulse width. As such, (3.33) implicitly accounts for the radar's pulse width in that the pulse width limits the size of the icebergs which the RCS describes.

In addition to the above dependencies, this form of the iceberg RCS also appears to show a dependence on the distance between the iceberg and the radar. This arises from the presence of the x_0^2 term as well as the $\rho_2 + \rho_1$ term in (3.33). The x_0^2 term may be removed by a simple conversion from polar to Cartesian coordinates. The distance dependency through the $\rho_2 + \rho_1$ term can also be shown to disappear under typical HFSWR operating conditions. Section 4.1 addresses this at length.

Chapter 4

Iceberg Radar Cross Section Simulation and Analysis

In Chapter 3, a RCS model for an iceberg region was derived. This RCS describes icebergs of any shape or size as long as the difference between the closest and furthest points of the iceberg, ρ_{min} and ρ_{min}, respectively, satisfy the condition $\rho_{\text{min}} - \rho_{\text{min}} < \frac{cT_r}{2}$. In this chapter, the effects of iceberg shape and size, as well as other parameters including radar operating frequency, on the RCS are studied via simulation.

In Section 4.1, the RCS equation given by (3.33) is converted to a form suitable for simulation. In Section 4.2, the simulation form of the RCS is modified for the case of rectangular icebergs. RCS simulation and analysis are then carried out in Sections 4.3 and 4.4 for square and rectangular icebergs, respectively. Section 4.5 contains a summary of the results of these simulations along with their implications.

4.1 Simulation Form of the Iceberg RCS Equation

The RCS of Equation (3.33) is currently in a form which is easily interpreted in terms of range and angle relative to the radar transmitter. For the purpose of simulation, it is favourable to express (3.33) in terms of Cartesian coordinates x, y. Figure 4.1 shows the iceberg region geometry once more, this time with Cartesian coordinates added.

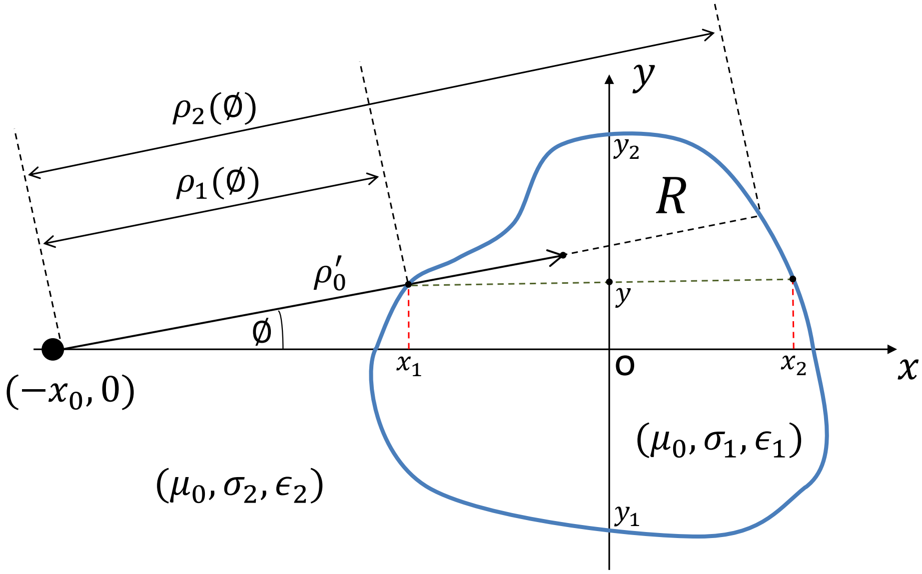

Figure 4.1: Iceberg geometry for simulation

In order to express (3.33) in terms of Cartesian coordinates, an assumption about the iceberg's dimensions relative to its distance from the radar must be made. In Section 3.4, it was assumed that the iceberg's maximum radial width was less than the patch width of the radar. As noted in that section, for a radar pulse width of 10 μs, the corresponding patch width is $cT_r/2 = 1500$ m. Consequently, icebergs with a maximum radial width of 1500 m could be observed. Here, it is now assumed that the distance x_0 to the iceberg from the radar is at least an order of magnitude larger than the observed iceberg's width. This assumption means the distance to the iceberg is on the order of tens of kilometers or larger, a reasonable assumption for a HFSWR system. With this assumption in place, consider the integral in (3.33) which is over the angle ϕ. The relationship between ϕ and y is, in general, given by $y = r \sin\phi$, where r is the distance from the transmitter to the point $(0, y)$. This relationship can be simplified if the angle, ϕ, is small over the integration range. Given that the iceberg distance from the radar is assumed to be an order of magnitude larger than the side length of the iceberg which faces the radar (the difference between y_2 and y_1) the small-angle approximation may be invoked giving $\sin\phi \approx \phi$. Furthermore, since ϕ is small, the distance from the transmitter to $(0, y)$ will be approximately constant and equal to x_0. Combining these observations results in

$$y \approx x_0 \phi \, . \tag{4.1}$$

Noting that $\phi \approx \frac{y}{x_0}$ and $d\phi \approx \frac{dy}{x_0}$, (3.33) may be written as a function of y,

$$\sigma \approx \frac{4}{\pi} \left| (\Delta_2 - \Delta_1) \int_{y_1}^{y_2} e^{-jk_0[\rho_2+\rho_1]} \sin\left[k_0(\rho_2 - \rho_1)\right] \, dy \right|^2 . \tag{4.2}$$

Referring to Figure 4.1 and again noting that the distance to the iceberg region is much greater than the size of the region, the difference between the closest and furthest points of the iceberg may be approximated as,

$$(\rho_2 - \rho_1) \approx (x_2 - x_1) \, , \tag{4.3}$$

where x_2 and x_1 are functions of y.

Next, consider the phase term, $e^{-jk_0[\rho_2+\rho_1]}$, in (4.2). The addition, $\rho_2 + \rho_1$, may be rewritten as,

$$\rho_2 + \rho_1 = 2\rho_1 + (\rho_2 - \rho_1) \approx 2\rho_1 + (x_2 - x_1)\,. \tag{4.4}$$

With the exception of the ρ_1 term, equation (4.4) is written in terms of Cartesian coordinates. It is also possible to write ρ_1 in terms of x and y. With reference to Figure 4.1, it is clear that ρ_1 is given by

$$\rho_1 = \frac{x_0 - |x_1|}{\cos\phi} = [x_0 - |x_1|] \cdot \sec\phi\,.$$

Recalling that $\sec^2\phi = 1 + \tan^2\phi$ and here $\tan\phi = \frac{y}{x_0 - |x_1|}$, $\sec\phi$ may be written as,

$$\sec\phi = \left[1 + \left(\frac{y}{x_0 - |x_1|}\right)^2\right]^{\frac{1}{2}}\,.$$

Therefore,

$$\rho_1 = [x_0 - |x_1|] \cdot \left[1 + \left(\frac{y}{x_0 - |x_1|}\right)^2\right]^{\frac{1}{2}}\,. \tag{4.5}$$

Using (4.3) and (4.4) in (4.2) a RCS equation expressed solely in terms of x, y is obtained as,

$$\sigma \approx \frac{4}{\pi}\left|(\Delta_2 - \Delta_1)\int_{y_1}^{y_2} e^{-jk_0[2\rho_1 + (x_2 - x_1)]}\sin\left[k_0(x_2 - x_1)\right]\,dy\right|^2 \tag{4.6}$$

where ρ_1 is given by (4.5).

Equation (4.6) may be furthered simplified by assessing the ρ_1 term in more detail.

Consider the $\left[1+\left(\frac{y}{x_0-|x_1|}\right)^2\right]^{\frac{1}{2}}$ portion of (4.5). This term may be rewritten as

$$\left[1+\left(\frac{y}{x_0-|x_1|}\right)^2\right]^{\frac{1}{2}} = \left[1+\left(\frac{\frac{y}{x_0}}{1-\frac{|x_1|}{x_0}}\right)^2\right]^{\frac{1}{2}} . \tag{4.7}$$

With reference to Figure 4.1 and equation (4.6), it is recalled that y is the variable of integration and ranges from y_1 to y_2. Furthermore, for a given y, $|x_1|$ is the distance from the origin to the iceberg edge which faces the radar. Since it is assumed that x_0 is at least an order of magnitude larger than the iceberg's extent in both the x and y directions, the ratios $\frac{y}{x_0}$, $\frac{|x_1|}{x_0}$ will be at maximum equal to 0.1. In this case, (4.7) will equate to 1.00615. For $\frac{y}{x_0}$ and $\frac{|x_1|}{x_0}$ decreasing in magnitude, (4.7) will further approach unity. As such, (4.7) may be approximated as unity and (4.5) can therefore be approximated as

$$\rho_1 \approx x_0 - |x_1| . \tag{4.8}$$

Equation (4.6) then becomes

$$\begin{aligned}\sigma &\approx \frac{4}{\pi}\left|(\Delta_2-\Delta_1)\int_{y_1}^{y_2} e^{-jk_0[2(x_0-|x_1|)+(x_2-x_1)]}\sin\left[k_0(x_2-x_1)\right]\,dy\right|^2 \\ &= \frac{4}{\pi}\left|(\Delta_2-\Delta_1)e^{-j2k_0x_0}\int_{y_1}^{y_2} e^{j2k_0|x_1|}e^{-jk_0(x_2-x_1)}\sin\left[k_0(x_2-x_1)\right]\,dy\right|^2\end{aligned} \tag{4.9}$$

where the exponential term involving x_0 has been removed from the integral as it does not depend on y. Noting that the magnitude of an exponential is equal to unity, the final form of the RCS is obtained as

$$\sigma \approx \frac{4}{\pi}\left|(\Delta_2-\Delta_1)\int_{y_1}^{y_2} e^{j2k_0|x_1|}e^{-jk_0(x_2-x_1)}\sin\left[k_0(x_2-x_1)\right]\,dy\right|^2 . \tag{4.10}$$

As alluded to in Section 3.5.2.1, the dependence on the distance x_0, which was seen in equation (3.33), has now been removed from the RCS expression. Additionally, the RCS has been converted from polar coordinates (ρ, ϕ) to Cartesian coordinates (x, y). Despite these changes, the new RCS expression of (4.10) still depends on the same physical parameters outlined in Section 3.5.2.1. These include:

- The geometry of the iceberg region,
- The electrical parameters of both the iceberg and the ocean surface,
- The operating frequency of the HFSWR system.

The effect of these parameters will be investigated throughout the rest of this chapter for the case of a rectangular shaped iceberg. Equation (4.10) will be used as the basis for all RCS simulations.

4.2 Iceberg RCS Equation for Rectangular Icebergs

In an effort to validate the RCS model derived in this thesis a rectangular model of the iceberg region is studied throughout the remainder of this chapter. Figure 4.2 shows a rectangular iceberg region. As in previous diagrams the figure depicts a top down view of the iceberg. In order to study how the proportions of an iceberg affect the RCS an aspect ratio has been defined in the figure that describes the relative side lengths of the rectangular iceberg. In particular, the aspect ratio is given as a/b where b is half the length of the side of the iceberg which is facing the radar and a is half the width of the iceberg.

Equation (4.10) may now be rewritten for the case of the rectangular iceberg. From Figure 4.2 it is clear that the limits on the integration variable y will be from

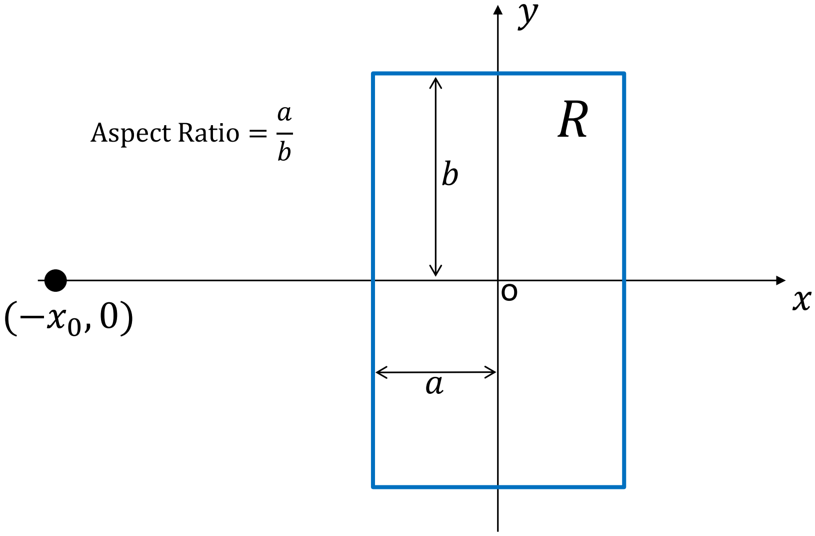

Figure 4.2: Rectangular iceberg geometry

$-b$ to b. Furthermore, for all y the difference $(x_2 - x_1)$ is constant and equal to $2a$. The $|x_1|$ term is also constant and is equal to a. Making these substitutions to (4.10) results in

$$\begin{aligned}\sigma &\approx \frac{4}{\pi}\left|(\Delta_2 - \Delta_1)\int_{-b}^{b} e^{j2k_0a}e^{-j2k_0a}\sin\left[2k_0a\right]\,dy\right|^2 \\ &= \frac{4}{\pi}\left|(\Delta_2 - \Delta_1)\int_{-b}^{b}\sin\left[2k_0a\right]\,dy\right|^2 .\end{aligned} \tag{4.11}$$

Noting that the sinusoid function in (4.11) is no longer a function of y it may be removed from the integral to simplify the expression. Doing this and carrying out the remaining integral gives

$$\begin{aligned}\sigma &\approx \frac{4}{\pi}\left|(\Delta_2 - \Delta_1)\cdot\sin\left[2k_0a\right]\int_{-b}^{b} dy\right|^2 \\ &= \frac{16b^2}{\pi}\left|(\Delta_2 - \Delta_1)\cdot\sin\left[2k_0a\right]\right|^2 .\end{aligned} \tag{4.12}$$

Several different parameters affect the value of the RCS. Referencing (4.12) it may be seen that, as expected, the values of a and b will have a large impact on the RCS value. The ratio of a to b is accounted for by the iceberg's aspect ratio. However, the actual values of a and b depend on the plan view area of the iceberg. The iceberg's plan view area is the area of the iceberg as shown in Figure 4.2. It is the area of the iceberg at height $z = 0$, i.e. the area of the iceberg which is in contact with the waterline. This area, A, can be written trivially in terms of a and b as $A = 4ab$. The effects of both the iceberg's shape (aspect ratio) and size (area) are detailed in Sections 4.3.1, 4.4.1, and 4.4.2.

The rectangular RCS is also dependent on the operating frequency of the radar as well as the electrical parameters of the iceberg and surrounding sea water. The operating dependency arises through the k_0 term in (4.12), since $k_0 = \omega_0/c$ and ω_0 is the radian operating frequency, and through the $(\Delta_2 - \Delta_1)$ term which is also a function of frequency (see Equations (2.17) - (2.20)). The effects of operating frequency on the RCS are covered in Section 4.3.2 and throughout Section 4.4. The RCS dependency on the electrical parameters, ϵ, σ, and μ, of both the iceberg and sea water is due to the $(\Delta_2 - \Delta_1)$ term in (4.12). Table 4.1 below shows the values used for these electrical parameters in all simulations which follow. These values are the same as those used in Walsh's simulation work [18].

	Relative Permittivity	Conductivity (S/m)
Iceberg	$\epsilon_{r_1} = 5$	$\sigma_1 = 10^{-5}$
Sea Water	$\epsilon_{r_2} = 80$	$\sigma_2 = 4$

Table 4.1: Electrical parameters used for simulations

4.3 Simulation and Analysis of the RCS for Square Icebergs

Before assessing the effects of differing aspect ratios, the special case of a square shaped iceberg is considered. A square iceberg has equal length sides implying $a = b$ and an aspect ratio of 1. Equation (4.12) can therefore be further simplified for the square iceberg case. If L is defined to be the length of one side of the square iceberg then $L = 2a = 2b$ and (4.12) can be written as

$$\sigma \approx \frac{4L^2}{\pi} \left|(\Delta_2 - \Delta_1) \cdot \sin\left[k_0 L\right]\right|^2 . \tag{4.13}$$

Simulations of the iceberg RCS for square shaped icebergs may now be carried out using (4.13). Section 4.3.1 contains an investigation of the effect that iceberg area has on the RCS magnitude and in Section 4.3.2 the impact of radar operating frequency is assessed. The electrical characteristics of the iceberg and sea water are given in Table 4.1.

4.3.1 Effect of Iceberg Area on Square RCS

Figure 4.3 shows a plot of the RCS of a square iceberg for iceberg areas ranging from $1\,\mathrm{m}^2$ to $10\,000\,\mathrm{m}^2$. Equation (4.13) was used to calculate the RCS for these different iceberg areas in order to understand how iceberg size affects the magnitude of the RCS. The RCS values in this figure have been normalized by dividing the RCS by the iceberg's plan view area L^2. The radar operating frequency for this plot is $f_0 = 25.4\,\mathrm{MHz}$.

The most striking features of this plot are the peaks and nulls that occur as the area

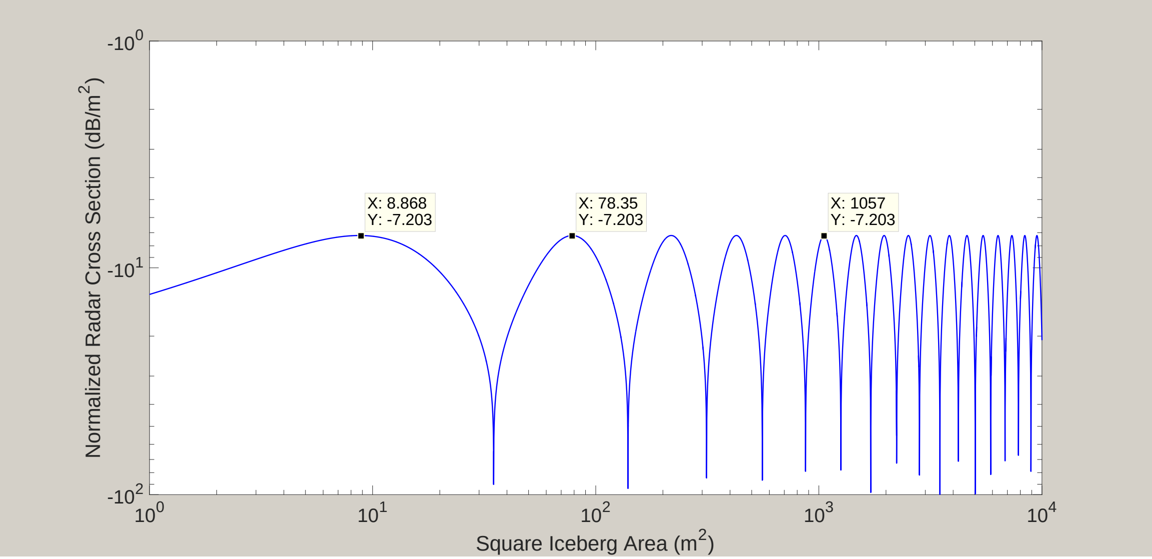

Figure 4.3: Backscattered RCS at 25.4 MHz for a square iceberg

of the iceberg changes. The most obvious explanation for their presence is constructive and destructive interference of the radar waves reflected off the leading and trailing edges of the iceberg. This would imply a relationship between the geometry of the iceberg and the wavelength of radar signal. Referring to (4.13), and noting that Figure 4.3 is a plot of the RCS normalized by the iceberg's area L^2, it obvious that the source of these peaks and nulls is the $\sin[k_0 L]$ term. In order to obtain the relationship between the radar's operating wavelength λ_0 and the iceberg's side length, this sinusoidal term may be rewritten as,

$$\begin{aligned} \sin[k_0 L] &= \sin\left[\frac{2\pi f_0 L}{c}\right] \\ &= \sin\left[\frac{2\pi L}{\lambda_0}\right] . \end{aligned} \tag{4.14}$$

The peaks in the RCS will occur whenever (4.14) is at a maximum. Since this is a sinusoidal function, it will have a maximum magnitude of 1 which occurs when

$\frac{2\pi L}{\lambda_0} = \frac{n\pi}{2}$, where n is a positive odd integer. Solving this maximum condition for the iceberg's side length gives the criteria for RCS peaks as

$$L = \frac{n\lambda_0}{4}, \quad \text{where } n \text{ is a positive odd integer.} \tag{4.15}$$

This peak criteria can be verified by investigating the side lengths corresponding to the RCS peaks in Figure 4.3. The first two RCS peaks correspond with iceberg areas of $8.868\,\mathrm{m}^2$ and $78.35\,\mathrm{m}^2$, respectively. The icebergs' side lengths, L, associated with these areas are $2.978\,\mathrm{m}$ and $8.852\,\mathrm{m}$, respectively. Noting that the operating frequency of 25.4 MHz used to generate Figure 4.3 implies a radar wavelength of $\lambda_0 = 11.811\,\mathrm{m}$, the ratio of the side length to operating wavelength (L/λ_0) gives approximately $\frac{1}{4}$ for the first peak and approximately $\frac{3}{4}$ for the second peak. These values clearly satisfy the peak criteria indicated in (4.15). Checking this with the 6th peak verifies this relationship. The iceberg at this peak has an area of $1057\,\mathrm{m}^2$ and a side length of $32.512\,\mathrm{m}$. The ratio of side length to wavelength here is equal to approximately $\frac{11}{4}$.

A similar criteria exists for the nulls. When the $\sin[k_0 L]$ term is at a minimum magnitude of 0, RCS nulls exist. The condition for this is $\frac{2\pi L}{\lambda_0} = n\pi$, where n is a positive integer. Again solving this minimum condition for the iceberg's side length gives the criteria for RCS peaks as

$$L = \frac{n\lambda_0}{2}, \quad \text{where } n \text{ is a positive integer.} \tag{4.16}$$

From the above mathematics this relationship between peaks/nulls and the operating wavelength should hold for all frequencies; only the value of the side lengths, or equivalently area, which satisfy the peak/null criteria, should change. Figure 4.4 shows another plot of normalized RCS against iceberg area. This time the radar operating frequency has been changed to $f_0 = 10.0\,\text{MHz}$.

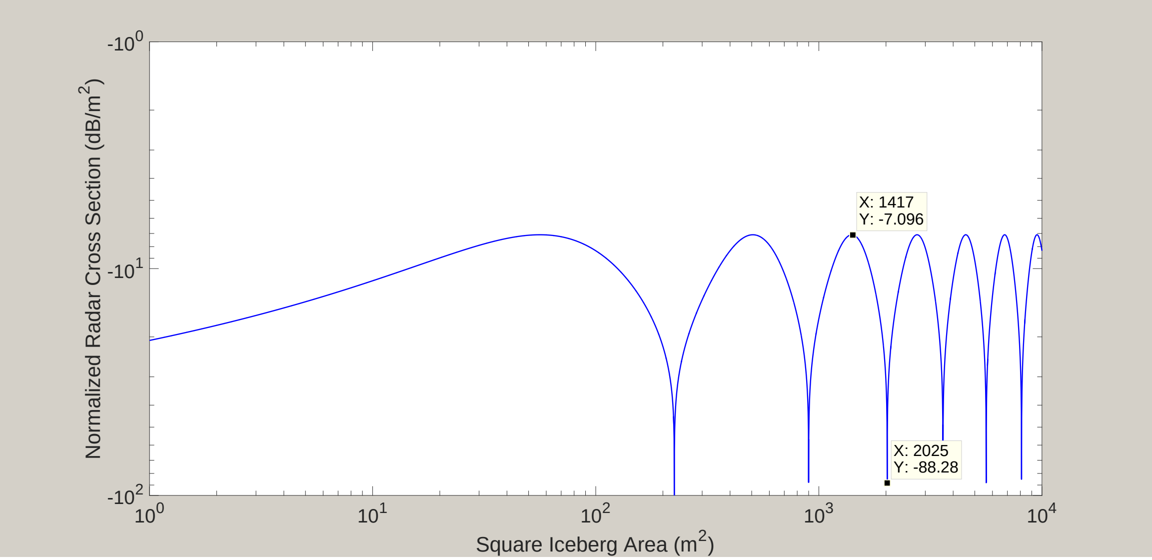

Figure 4.4: Backscattered RCS at 10.0 MHz for a square iceberg

As expected the same peak/null relationship to wavelength exists for this operating frequency. The wavelength for a 10.0 MHz signal is ~30 m. Considering the third peak, the iceberg corresponding to this peak has an area of $1417\,\text{m}^2$ and a side length of 37.643 m which implies a side length to wavelength ratio of $\frac{5}{4}$. The third null corresponds to an iceberg with an area of $2025\,\text{m}^2$ with a side length of 45.000 m, giving a side length to wavelength ratio of $\frac{3}{2}$. Note that because the wavelength is longer in this simulation there are fewer peaks and nulls for the same range of iceberg sizes.

Similar simulations to those in Figures 4.3 and 4.4 were undertaken in [19]. In [19] both the second-order and first-order components of a square RCS were simulated. This is in contrast to the results presented here, which consider only the first-order component of the RCS. Another difference between the simulations in [19] and those presented here is that no transmit waveform is explicitly specified in [19]. In this thesis a pulsed sinusoid waveform is assumed. Despite these differences the plots of normalized RCS against iceberg area have a very similar trend and magnitude. Moreover, the same peak/null relationship between iceberg side length and wavelength exists in both works. In [19] the authors make the observation that RCS peaks occur when the perimeter of the iceberg is an odd integer multiple of wavelength $(= \lambda_0, 3\lambda_0, 5\lambda_0, \ldots)$. Similarly the authors state that RCS nulls occur when the perimeter of the iceberg is an even integer multiple of wavelength $(= 2\lambda_0, 4\lambda_0, 6\lambda_0, \ldots)$. Since the perimeter, P, of a square iceberg is equal to four times the side length $(P = 4L)$, their statement is equivalent to the criteria of (4.15) and (4.16).

Another notable feature of Figures 4.3 and 4.4 is that, for a particular operating frequency, the RCS magnitude at the peaks are identical. This is only the case for the normalized RCS. This normalization allows the RCS to be plotted on a similar magnitude scale for different iceberg areas, but it is important to note that the RCS magnitude at a peak increases as iceberg area increases. This result is expected since, for all other iceberg properties being identical, a larger iceberg should backscatter more of the incident radiation to the receiver.

4.3.2 Effect of Operating Frequency on Square RCS

As noted in Section 4.2 the iceberg RCS has a dependence on the radar operating frequency through the k_0 and $(\Delta_2 - \Delta_1)$ terms in (4.13). The plots in Section 4.2, Figures 4.3 and 4.4, provide some insight to the frequency dependence of the RCS. Figure 4.3 shows the RCS for an operating frequency of 25.4 MHz while Figure 4.4 is for an operating frequency of 10.0 MHz. The RCS peaks have almost the same magnitude. For $f_0 = 25.4\,\text{MHz}$ the RCS peak magnitude is $-7.203\,\text{dB}$, while the $f_0 = 10.0\,\text{MHz}$ case has a RCS peak magnitude of $-7.096\,\text{dB}$. A difference of about

0.107 dB in magnitude. This would suggest that the RCS has only a slight dependence on radar operating frequency.

To isolate the effect which operating frequency has on the square iceberg RCS, simulations have been carried out for a fixed iceberg size (area) while the operating frequency is varied from 3 MHz to 30 MHz.

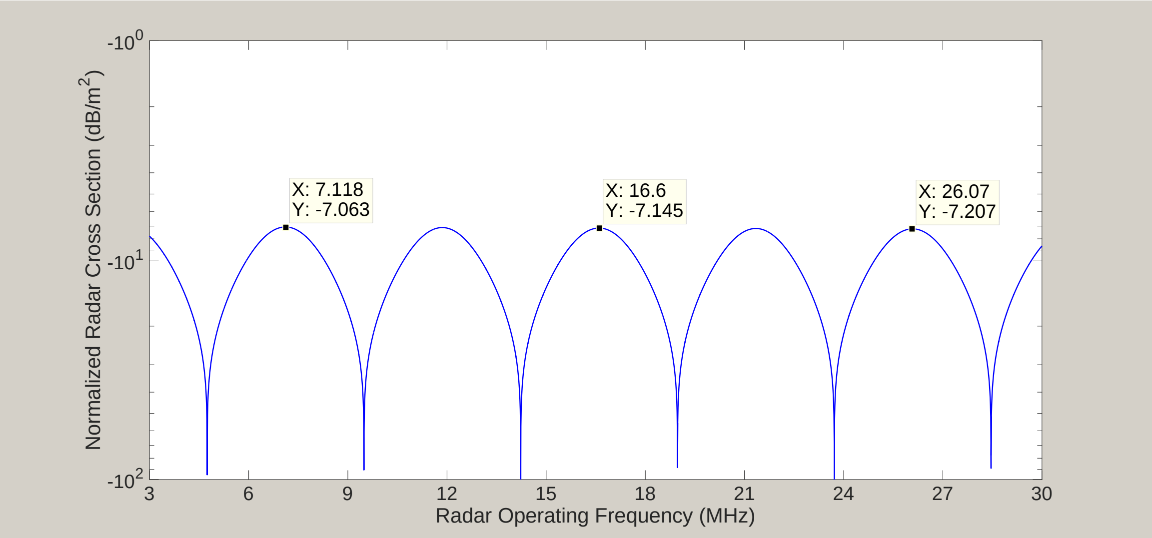

Figure 4.5: Backscattered RCS as function of operating frequency for a square iceberg with area of 1000 m^2

Figure 4.5 is for a square iceberg with area 1000 m^2 while Figure 4.6 is for an iceberg with an area of 10 000 m^2. From the figures it is observed that as the radar operating frequency increases, the RCS peak magnitude decreases slightly. Referring to (4.13), it is evident that the source of the RCS magnitude change is due to the surface impedance term $(\Delta_2 - \Delta_1)$ and not the k_0 term. Although k_0 is also frequency dependent, it is contained within a sine function which will have the same maximum value of unity at a RCS peak. Therefore the frequency dependence must arise from the $(\Delta_2 - \Delta_1)$ term. This surface impedance term does not modify the RCS magnitude substantially. In Figure 4.6, for example, the RCS peak magnitude changes

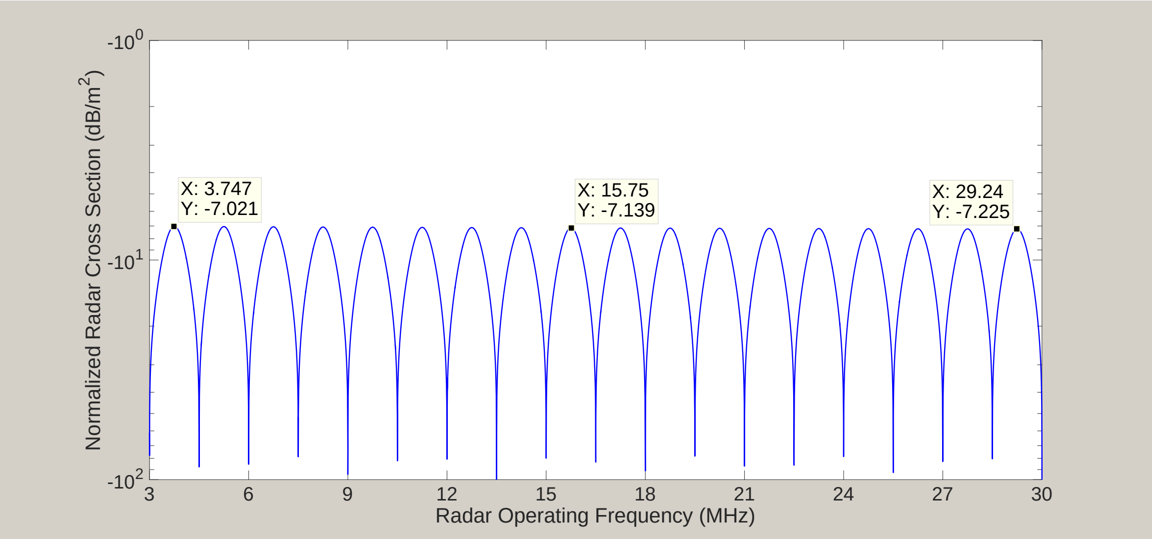

Figure 4.6: Backscattered RCS as function of operating frequency for a square iceberg with area of 10 000 m^2

from $-7.021\,\mathrm{dB}$ at $3.747\,\mathrm{MHz}$ to $-7.225\,\mathrm{dB}$ at $29.24\,\mathrm{MHz}$. This small change is to be expected since in Section 3.1.2 it was noted that $(\Delta_2 - \Delta_1)$ varies slowly with frequency. The simulations carried out for Figures 4.5 and 4.6 confirm this.

Although the k_0 term does not affect the RCS peak magnitude, it does play a role in the location of the peaks/nulls. This is reflected in Figures 4.5 and 4.6. These figures demonstrate the same peak/null pattern as the figures in Section 4.3.1. For nulls to occur, the side length has to satisfy the relationship $L = \frac{n\lambda_0}{2}$ where n is a positive integer. Here, the side length is now fixed and nulls will occur whenever the wavelength $\lambda_0 = \frac{2L}{n}$. A similar relationship can be found for the peaks as well. This relationship, explains why there are more peaks/nulls in Figure 4.6 than in Figure 4.5. Rewriting the null criteria in terms of frequency gives, $f_0 = \frac{nc}{2L}$. Thus, for a larger iceberg there will be more frequencies which satisfy the null (or peak) criteria for a given range of frequencies.

4.4 Simulation and Analysis of the RCS for Rectangular Icebergs

The case of equal-side-length icebergs was analyzed in Section 4.3. Here, the effect of changing iceberg shape is investigated. This is carried out by varying the aspect ratio of the iceberg, while keeping the iceberg area constant. Figure 4.2 indicates that icebergs which have aspects ratios of less than unity have larger b than a, meaning that the side length facing the radar is larger than the width of the iceberg. Conversely, aspect ratios greater than unity correspond to icebergs which have larger a than b and hence a longer width than length.

In Section 4.4.1, the RCS is simulated for several different aspect ratio and operating frequency combinations against iceberg area. In Section 4.4.2, the effect of the aspect ratio on the RCS is isolated by varying it while keeping both the operating frequency and iceberg area constant. The electrical characteristics of the iceberg and sea water are again given in Table 4.1.

4.4.1 Effect of Iceberg Area on Rectangular RCS

In this section, the RCS is plotted as a function of area as was done in Section 4.3.1. The same operating frequencies of 25.4 MHz and 10 MHz are used here. However, this time the aspect ratios of the icebergs are 4 and 0.25. This means that one side of the iceberg is four times the length of the other. For an aspect ratio of 4, the width of the iceberg is four times the side length which faces the radar ($a = 4b$). For an aspect ratio of 0.25, the side facing the radar is four times the iceberg's width ($b = 4a$).

Simulations for rectangular icebergs use the rectangular RCS equation (4.12), which was derived in Section 4.2. In Section 4.3.1 it was shown that the sine term in the square iceberg RCS equation (4.13) leads to peaks/nulls in the RCS. A similar sine term exists in the more generalized rectangular RCS equation. Comparing this to the sine term for the square case in (4.13), the locations of the peaks and nulls for rectangular icebergs may be predicted. Substituting $2a$ for L in (4.15) and (4.16) gives the criteria for RCS peaks and nulls for rectangular icebergs. For peaks to occur, the iceberg width must satisfy the following condition,

$$2a = \frac{n\lambda_0}{4}, \quad \text{where } n \text{ is a positive odd integer.} \tag{4.17}$$

Similarly for nulls,

$$2a = \frac{n\lambda_0}{2}, \quad \text{where } n \text{ is a positive integer.} \tag{4.18}$$

Figure 4.7 show a plot of normalized RCS against area for an iceberg aspect ratio of 4 and an operating frequency of 25.4 MHz.

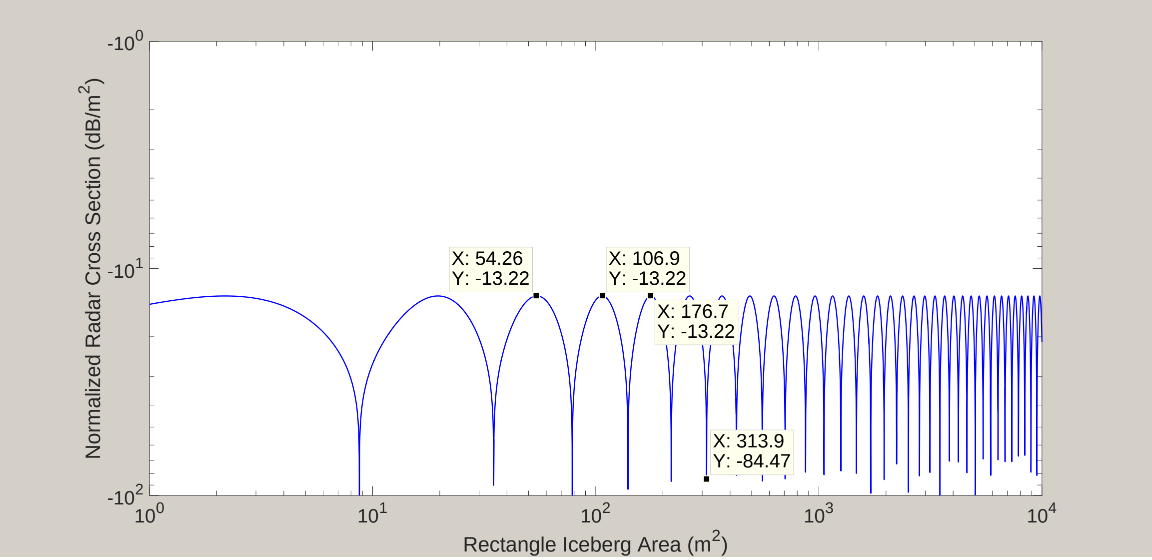

Figure 4.7: Backscattered RCS at 25.4 MHz for a rectangular iceberg with aspect ratio of 4

To test the predictions of (4.17) and (4.18) consider the third, fourth, and fifth RCS peaks. These correspond to iceberg areas of $54.26\,\mathrm{m}^2$, $106.9\,\mathrm{m}^2$, and $176.7\,\mathrm{m}^2$. The width of the iceberg, $2a$, has values of 14.732 m, 20.679 m, and 26.586 m for these areas. From (4.17) it is expected that the iceberg width to wavelength ratios, $2a/\lambda_0$, for the third, fourth, and fifth peaks are $\frac{5}{4}$, $\frac{7}{4}$, and $\frac{9}{4}$. Recalling that the wavelength for a 25.4 MHz signal is 11.811 m, the ratios calculated from the plot are 1.247, 1.751, and 2.251 as expected. The criteria for RCS nulls can be verified in a similar manner. Consider the sixth null in Figure 4.7. The iceberg area and width corresponding to this null are $313.9\,\mathrm{m}^2$ and 35.434 m, respectively. The width to wavelength ratio is thus 3.00 as (4.18) predicts.

Figure 4.8 shows simulation results for icebergs with an aspect ratio of 0.25. The operating frequency has been maintained at 25.4 MHz. It possible to show that the same peak/null criteria given by (4.17) and (4.18) still hold for this different aspect ratio, as expected from equation (4.12).

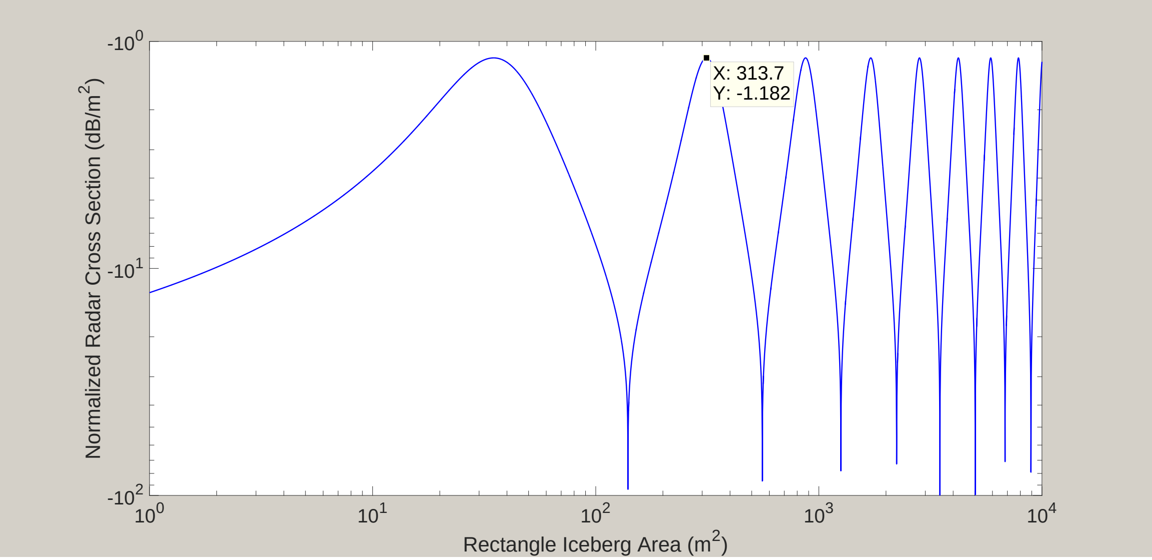

Figure 4.8: Backscattered RCS at 25.4 MHz for a rectangular iceberg with aspect ratio of 0.25

Comparing Figures 4.8 and 4.7 there are several notable differences. The first is the number of peaks/nulls. There are fewer peaks/nulls for the 0.25 aspect ratio rectangular icebergs. This is a direct consequence of the fact that for smaller aspect ratios the $2a$ dimension or width of the iceberg will have a smaller range of values for the same set of iceberg areas as compared to a larger aspect ratio. Since $2a$ in equations (4.17) and (4.18) takes on a smaller range there are fewer multiples of the wavelength which satisfy the null/peak criteria. The second major difference between the 0.25 and 4 aspect ratio plots is that the magnitude of the peaks is substantially larger for the smaller aspect ratio. The peaks in Figure 4.8 have a magnitude of approximately $-1.182\,\mathrm{dB}$. In Figure 4.7 the peaks have a magnitude of approximately $-13.220\,\mathrm{dB}$. For the square iceberg case shown in Figure 4.3 the peaks have a magnitude of approximately $-7.203\,\mathrm{dB}$. For the square case the aspect ratio is 1. It can therefore be concluded that as the aspect ratio decreases the magnitude of the signal returned to the radar increases. This makes good physical sense since as the aspect ratio decreases the b dimension increases meaning more of the iceberg is facing the radar and able to reflect the transmitted signal for the same iceberg area.

Figures 4.9 and 4.10 show two more plots of the RCS against iceberg area. The aspect ratios for these figures are again 4 and 0.25, respectively. However, the operating frequency has been changed to 10.0 MHz. For the same aspect ratio the peaks have a slightly larger magnitude for the 10.0 MHz case. This slight dependence on operating frequency was also noted for the square iceberg case in Section 4.3.2 and is due to the surface impedance term $(\Delta_2 - \Delta_1)$ in (4.12).

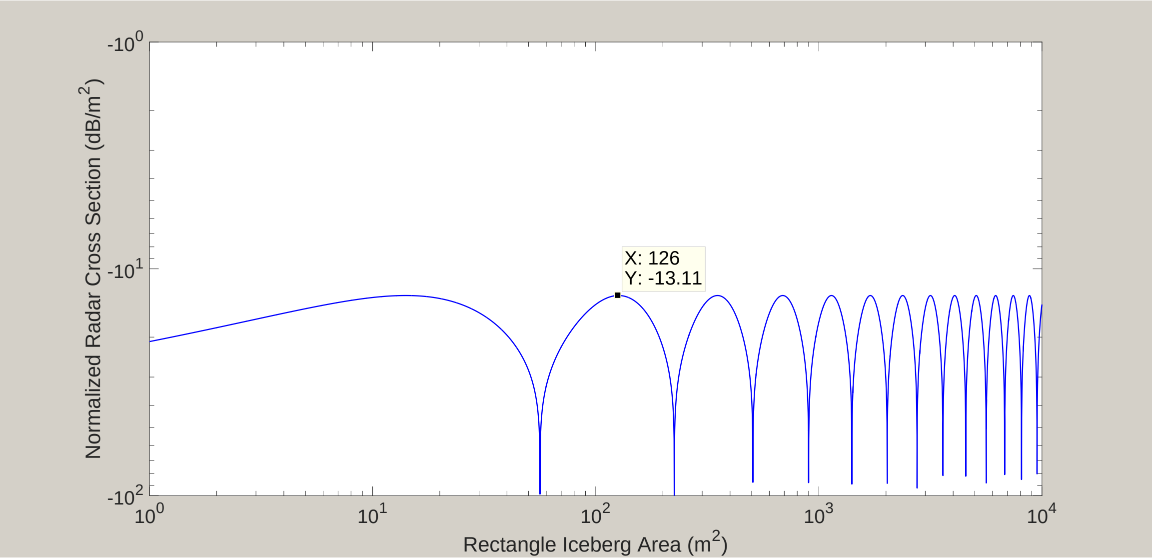

Figure 4.9: Backscattered RCS at 10.0 MHz for a rectangular iceberg with aspect ratio of 4

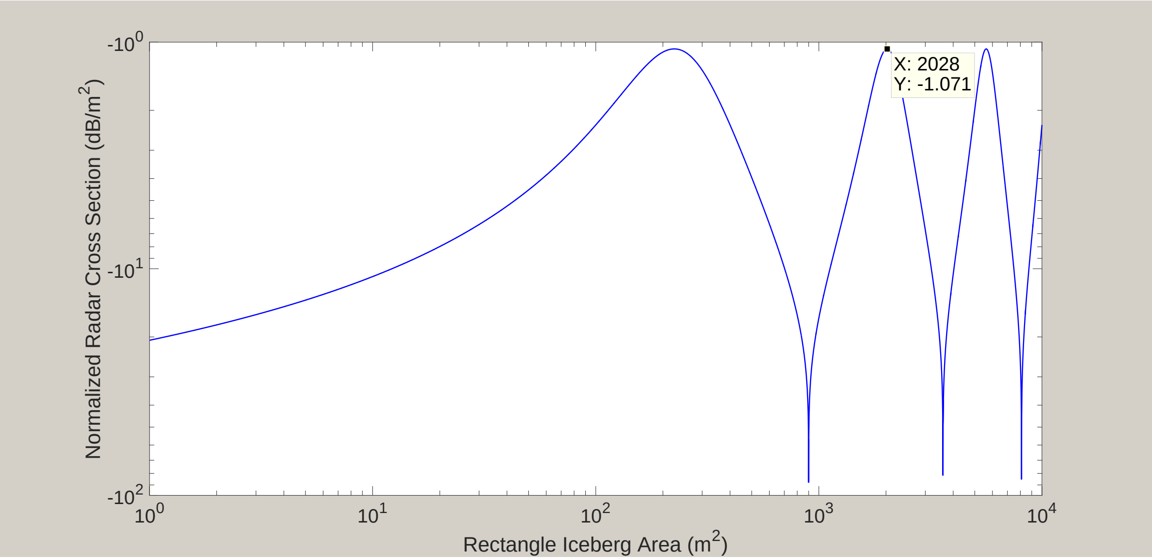

Figure 4.10: Backscattered RCS at 10.0 MHz for a rectangular iceberg with aspect ratio of 0.25

4.4.2 Effect of Aspect Ratio on Rectangular RCS

It was found in Section 4.4.1 that as the iceberg's side length which faces the radar increases so does the magnitude of the RCS. This side length is given by $2b$ as depicted in Figure 4.2. This relationship is not surprising since the rectangular RCS equation (4.12) is proportional to b^2 and hence is proportional to the iceberg's side length which faces the radar. To study this relationship further the RCS is now simulated as a function of aspect ratio while the operating frequency and iceberg area are fixed.

Figure 4.11 plots normalized RCS against aspect ratios ranging from 0.25 to 4. The iceberg area for this simulation is $1000\,\mathrm{m}^2$ and the operating frequency is 25.4 MHz.

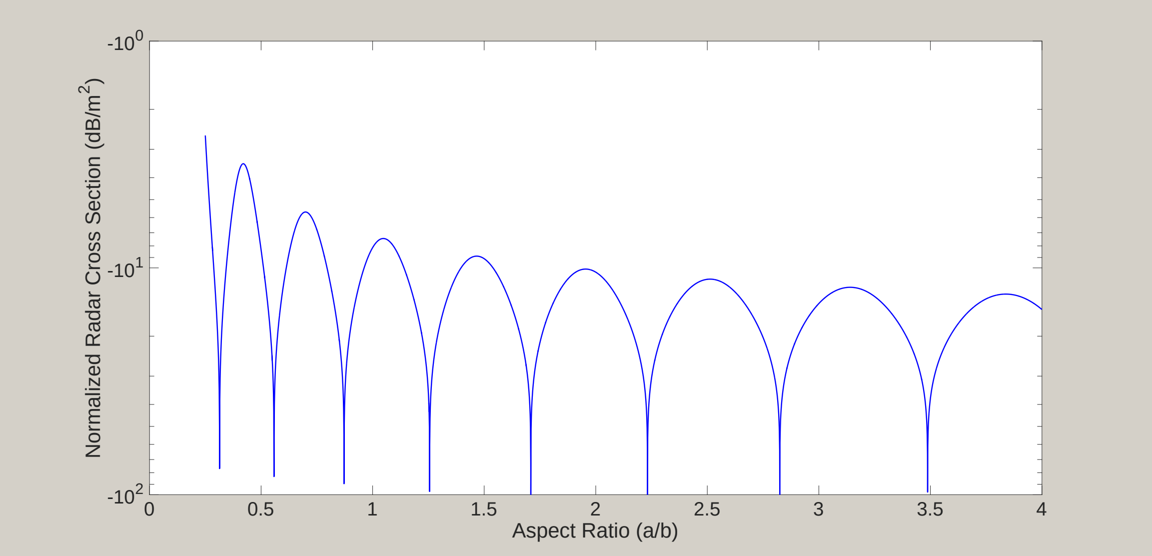

Figure 4.11: Backscattered RCS at 25.4 MHz for a rectangular iceberg with area $1000\,\mathrm{m}^2$

Firstly, it may be noticed that the same peak and null features seen in previous simulations are still present here. This is because varying the aspect ratio while the area is fixed will result in the iceberg width changing in size and there will be several widths which satisfy the peak/null criteria of (4.17) and (4.18). Secondly, Figure 4.11 shows the expected trend between the RCS magnitude and the iceberg's side length $2b$. If only the RCS magnitude at the peaks is considered the RCS magnitude increases as the aspect ratio decreases. Of course as the aspect ratio decreases b is increasing and thus more of the iceberg is facing the radar. Since Figure 4.11 shows a plot of the RCS on a logarithmic scale the change in RCS magnitude with aspect ratio is quite substantial. To verify this trend for a different iceberg area Figure 4.12 shows the same plot as above but this time for a iceberg area of 10 000 m^2. Here, as expected, the trend is again evident.

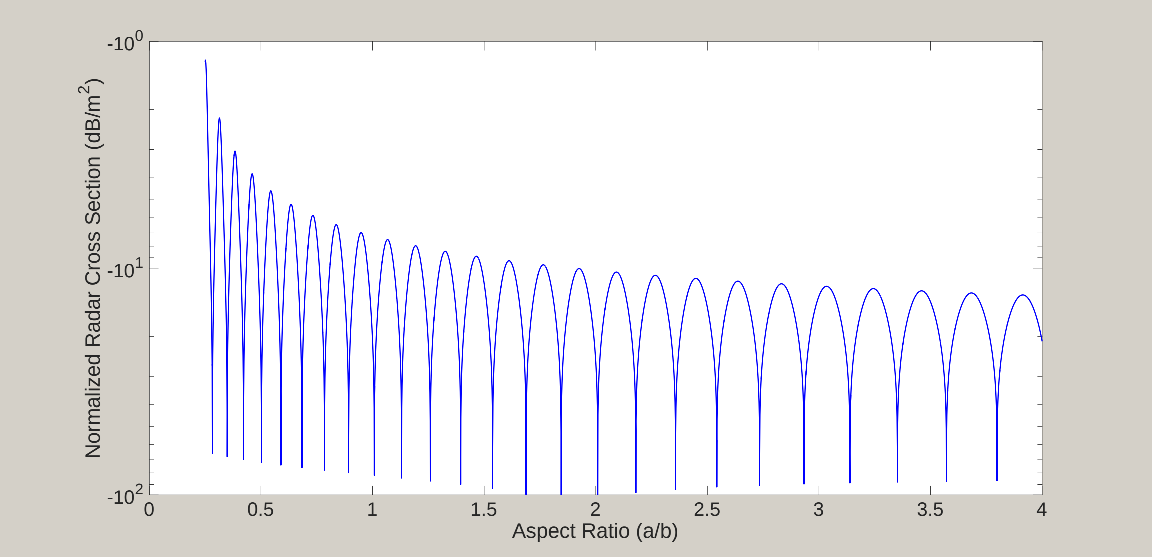

Figure 4.12: Backscattered RCS at 25.4 MHz for a rectangular iceberg with area 10 000 m^2

The fact that rectangular RCS is proportional to the square of the iceberg side length which faces the radar is an important conclusion. It it shown in [29] that the RCS of a rectangular plate for a vertically polarized radar is proportional to this side length squared, i.e to b^2. The result obtained in this thesis is consistent with this research even though the RCS derived here is for an arbitrary shaped iceberg region. This helps to support and validate the RCS equation given by (3.33). Applying this equation to the specific case of a rectangular iceberg region has led to the same result found in research focusing on the rectangular RCS specifically.

4.5 Conclusions Based on Rectangular Simulations

Sections 4.2 - 4.4 contained an analysis of the RCS for rectangular icebergs. Here, the main findings of this analysis are summarized and interpreted.

The most significant findings relate to the geometry of the rectangular iceberg. With reference to Figure 4.2, it is recalled that a is a measure of the iceberg's width, i.e. the side length which is in-line, or parallel, with the radar's look direction. The other side length which is facing, and perpendicular to, the radar's look direction is given by b. It was found that as b increased in size, the magnitude of the RCS peaks also increased. It was noted that this is not surprising since the RCS equation for a rectangular iceberg, given by (4.12), is proportional to b^2. However, this is an important conclusion since intuitively it makes sense that as b increases the RCS magnitude also increases as there is more of the iceberg facing the radar and able to reflect the incident electromagnetic energy back to the radar. In contrast, the side length a was found to have no effect on the magnitude of the RCS peaks, but instead affected the condition under which the peaks/nulls would occur. This also makes good physical sense. As the width of the iceberg changes, there will be differing amounts of constructive and destructive interference due to reflections off the leading and trailing edges of the iceberg for a particular operating frequency.

As noted above, the largest impact on the RCS for a rectangular iceberg comes from the iceberg's geometry. However, the operating frequency of the radar also plays a role on the RCS. For a fixed side length a, the operating frequency will determine when RCS peaks/nulls occur. This is because a particular operating frequency corresponds to a particular signal wavelength which again leads to varying amounts of constructive and destructive interference. The operating frequency also had a small impact on the magnitude of the RCS. This was determined to be due to the surface impedance term $(\Delta_2 - \Delta_1)$ which also depends on frequency. It was found that as operating frequency increases the surface impedance decreased, and this led to a lower magnitude RCS. However, the change in magnitude due to this was fairly small over the simulated frequency range of 3.0 MHz to 30.0 MHz. This is a direct consequence of the fact that the surface impedance term varies slowly with frequency.

Chapter 5

Conclusions

5.1 General Synopsis and Significant Results

The development of a new analytical iceberg RCS model for a pulsed HFSWR system has been accomplished in this thesis. Using this RCS model, simulations have been performed on rectangular-shaped icebergs in order to test the validity of the RCS expression. The starting point for this thesis can be found in early HFSWR iceberg work by Walsh [5], where general electric field equations for an iceberg region were established.

In order to provide a background for the RCS derivation carried out in this thesis, the analysis started with an overview of Walsh's work [5]. Maxwell's equations were applied to a space representing an iceberg region surrounded by water with free space above these media. Under the assumption of a vertical dipole source, the vertical component of the general electric equations for the space as found by Walsh were stated. The analysis then deviated from Walsh's work and the appropriate general field equation was separated into first and second-order field components. The two-dimensional spatial convolutions in both the first and second-order equations were then written explicitly. This facilitated an analysis and discussion of the physical scattering mechanisms involved in each expression. It was found that the first-order electric field equation involves a single scatter of the transmitted signal off the iceberg region before the signal travels to the observation point (receiver). Meanwhile, the second-order electric field equation involves two scatters off the iceberg region before propagating to the observation point.

The RCS derivation then focused solely on the first-order electric field equation. It was assumed that the radar system under consideration was a monostatic radar system. As such, the first-order electric field equation was evaluated at the coordinates of the transmit antenna to give an initial form of the backscattered field equation. This equation was then inverse Fourier transformed, resulting in a time domain expression for the backscattered electric field. In order to complete this inverse transform, it was assumed that both the Sommerfeld attenuation function and the surface impedance terms varied slowly over the frequency band of interest. The resulting time domain expression allows for any time domain current excitation waveform to be specified.

As indicated above, the analysis in this thesis focused on a pulsed sinusoid waveform for the excitation current. After inserting this excitation current waveform, and simplifying the resulting backscattered field equation, a two-dimensional coordinate transform was performed which converted the equation from Cartesian coordinates to the more radar-appropriate polar coordinates. By assessing the times for which the backscattered electric field was non-zero it was demonstrated from a time domain perspective that the first-order backscattered field equation indeed describes single scattering off the iceberg region. Finally, by assuming that the iceberg observed by the HFSWR fits within a single radar pulse width the backscattered field equation was simplified to its final form.

Before the iceberg RCS equation could be obtained, the power received by the HFSWR was calculated using the final form of the backscattered electric field. A comparison between the power received and the standard monostatic radar range equation then gave the desired iceberg RCS equation. The iceberg RCS equation was found to depend on a number of iceberg and radar parameters. As expected, the largest dependence was on the geometry of the iceberg itself. Additionally, the iceberg RCS also takes into account the electrical parameters of the iceberg and the surrounding ocean surface, as well as the operating frequency of the HFSWR system. Initially, the RCS appeared to be dependent on the distance between the iceberg and the radar. However, this dependence was shown to disappear as long as the distance to the iceberg from the radar was an order of magnitude larger than the dimensions of the iceberg itself. Given that it was earlier assumed that the iceberg is contained within a single radar patch width, this is a reasonable assumption for a HFSWR system.

In order to validate the iceberg RCS expression, simulations of the RCS were carried out for the case of rectangularly shaped icebergs. Several important conclusions were found. The first of these was the occurrence of peaks and nulls in the normalized RCS when plotted against iceberg area. The criteria for the peak/nulls was determined and found to be the result of constructive and destructive interference between reflections off the leading and trailing edges of the iceberg. As such, only the width of the iceberg and the operating frequency, or equivalently wavelength, affected the occurrence of peaks/nulls. Previous research by Walsh et al [19] for square icebergs found the same relationship for peaks/nulls as was obtained in this thesis even though a plane wave excitation was assumed for the simulations in [19]. Another important observation was the fact that the rectangular iceberg RCS was proportional to the square of the side length which faces the radar (i.e. side which is perpendicular to the radar's look direction). Not only does this make intuitive sense in that as more iceberg is available to reflect the incident fields the RCS magnitude increases, it also agrees with previous research which focuses on the RCS of a rectangular plate [29]. Finally, it was also noted that the RCS has a slight dependency on radar operating frequency. However, this dependence is small since it arises from the surface impedance terms which vary slowly with frequency.

5.2 Overview of Iceberg RCS Model Assumptions

In obtaining the iceberg RCS model derived in this thesis, several assumptions have been made regarding the iceberg under observation. This section briefly highlights these assumptions and any potential limitations of the derived iceberg RCS model as a result of these assumptions.

The starting point of the iceberg RCS derivation is the application of Maxwell's equations to the space shown in Figure 2.1. This model makes two assumptions about the iceberg region. The first is that the iceberg is infinite in depth below the ocean surface. The second is that the iceberg region has no height above the ocean surface. In reality, an iceberg will of course have both a finite depth and also a non-zero height above the ocean surface. Consequently, it is natural to question the real-world applicability of the RCS model derived here. However, these assumptions can be justified for a HFSWR system. A HF radar signal operating in surface-wave mode over the ocean surface has an electric field intensity that is essentially confined to the conducting ocean surface. Underneath the ocean surface the electric field intensity drops off drastically due to the skin depth effect. As such, a HFSWR does not "see" the portion of the iceberg located underneath the ocean surface and the backscattered field is largely independent of the iceberg's depth below the ocean surface. Similarly, the electric field intensity above the waterline is also quite small. As a result, the largest portion of the backscattered field is due to the change in electrical properties between the ocean and the iceberg at the height of the ocean's surface. Despite this, quantifying the effect of having non-zero iceberg height would be an interesting subject of future work.

Another major assumption used in the derivation of the iceberg RCS model is that the distance x_0 between the iceberg and the radar is much larger than the maximum radial width of the iceberg. This assumption is very common in analytical HFSWR research (see, for example, [21]) because the observable patch width of a pulsed HFSWR system is on the order of a few kilometers, at maximum, while the radar has an operating range on the order of hundreds of kilometers. However, it should be mentioned that as a result of this assumption the iceberg RCS model derived here will begin to lose accuracy as the distance to the iceberg approaches the size of the iceberg, i.e. a large iceberg located near the transmit antenna. However, in such a situation the iceberg would be close enough to detect using other methods, such as marine radar.

5.3 Suggestions for Future Work

There are several obvious extensions to the work presented in this thesis. Most significantly, this thesis focuses only on the first-order component of the backscattered electric field. Future work could focus on obtaining a backscattered electric field equation, and corresponding RCS, for the second-order field component given by (2.34). The combined effects of both the first-order and second-order RCS could then be simulated and compared against the RCS obtained in this thesis.

Another obvious extension of this thesis is the exploration of different excitation waveforms. Equation (3.8) is general in the sense that any time domain current excitation waveform may be specified. Modern HFSWR systems often use a FMCW as their excitation waveform. By simply replacing the pulsed sinusoid current used here with the time domain FMCW current waveform, a new backscattered electric field and RCS could be derived.

This thesis makes use of simulation to assess how the derived iceberg RCS behaves and also to help validate the RCS expression. Ultimately, the derived iceberg RCS can only truly be validated by comparison to field data. By using ground truth data for icebergs, simulations could be carried out and compared against actual HFSWR returns. This would provide insight into the accuracy of the derived RCS model. Additionally, inversion techniques, based on the iceberg RCS equation derived in this thesis, could be developed and used to extract information about an iceberg under observation including its location, size, and direction of travel. This could also be compared against field data.

The iceberg RCS derivation presented in this thesis was based on Walsh's initial work in [5]. As detailed in the problem formulation section of this thesis, Walsh assumed that the iceberg region was flat and has no height above the water line. The basis of this assumption was that the majority of the backscattered signal is due to the change in electrical parameters between the iceberg and ocean media. Since Walsh's general electric field equations are used as a starting point for this thesis' derivation, this assumption is present in this analysis as well. In reality, all icebergs have a finite height above the ocean surface. As such, an area of future research could be to derive from first principles the electric field expressions for an iceberg with a non-zero height.

Bibliography

[1] Noaa.gov, "NOAA - National Oceanic and Atmospheric Administration - Ocean," 2015, [Accessed: 15-February-2015]. [Online]. Available: http://www.noaa.gov/ocean.html

[2] W. Lord, *A Night to Remember*, ser. Holt Paperback. New York: Henry Holt and Company, 1955.

[3] S. Srivastava and J. Walsh, "Over-the-horizon radar," in *Remote Sensing of Sea Ice and Icebergs*, S. Haykin, Ed. New York: Wiley, 1994, pp. 299–339.

[4] E. D. R. Shearman, "Radio science and oceanography," *Radio Science*, vol. 18, no. 3, pp. 299–320, 1983.

[5] J. Walsh, "Electromagnetic propagation and scatter for mixed paths with multiple and finite discontinuities and application to remote sensing of sea ice with HF radar," Memorial Univ. of Newfoundland, St. John's, Nfld., Canada, C-CORE Tech. Rep. 83-16, 1983.

[6] G. Millington, "Ground-wave propagation over an inhomogeneous smooth earth," *Proceedings of the IEE - Part III: Radio and Communication Engineering*, vol. 96, no. 39, pp. 53–64, January 1949.

[7] P. C. Clemmow, “Radio propagation over a flat earth across a boundary separating two different media,” *Trans. Royal Soc. (London)*, vol. 246, no. 905, pp. 1–55, June 1953.

[8] H. Bremmer, “The extension of Sommerfeld’s formula for the propagation of radio waves over a flat earth to different conductivities of the soil,” *Physica’s Grav*, vol. 20, p. 441, 1954.

[9] J. R. Wait, “Electromagnetic surface waves,” in *Advances in Radio Research*, J. A. Saxton, Ed. New York: Academic Press, 1964, vol. 1, pp. 157–170.

[10] J. R. Wait, “Propagation of electromagnetic waves over a smooth multisection curved earth-an exact theory,” *Journal of Mathematical Physics*, vol. 11, no. 9, pp. 2851–2860, 1970.

[11] J. R. Wait, *Electromagnetic Waves in Stratified Media.* New York: Pergamon Press, 1970.

[12] J. R. Wait, “Recent analytical investigations of electromagnetic ground wave propagation over inhomogeneous earth models,” *Proceedings of the IEEE*, vol. 62, no. 8, pp. 1061–1072, Aug 1974.

[13] J. Ryan, “The electromagnetic scattering from a vertical discontinuity with applications to ice hazard detection - an operator expansion approach,” Master’s thesis, Memorial University of Newfoundland, St. John’s, NL, Canada, 1983.

[14] J. Walsh, “On the theory of electromagnetic propagation across a rough surface and calculations in the VHF region,” Memorial Univ. of Newfoundland, St. John’s, Nfld., Canada, OEIC Report N00232, 1980.

[15] J. Walsh, "A general theory of the interaction of electromagnetic waves with isotropic, horizontally layered media and applications to propagation over sea ice," Memorial Univ. of Newfoundland, St. John's, Nfld., Canada, C-CORE Tech. Rep. 82-9, 1982.

[16] J. Ryan and J. Walsh, "Electromagnetic scattering from a vertical discontinuity with application to ice hazard detection," in *IEEE Antennas and Propagation Society International Symposium, 1983*, vol. 21, May 1983, pp. 469–472.

[17] J. Ryan and J. Walsh, "Electric dipole fields over a quarter space earth inhomogeneity and application to ice hazard detection," *Radio Science*, vol. 20, no. 6, pp. 1518–1528, 1985.

[18] J. Walsh and S. K. Srivastava, "Model development for feasibility studies of HF radars as ice hazard remote sensors," Memorial Univ. of Newfoundland, St. John's, Nfld., Canada, OEIC Tech. Rep. N00397, 1984.

[19] J. Walsh, B. Dawe, and S. K. Srivastava, "Remote sensing of icebergs by groundwave doppler radar," *Oceanic Engineering, IEEE Journal of*, vol. 11, no. 2, pp. 276–284, Apr 1986.

[20] J. Walsh, R. Howell, and B. Dawe, "Model development for evaluation studies of ground wave radar," Centre for Cold Ocean Resources Engineering, St. John's, Nfld., Canada, Contract Report 90-C14, 1990.

[21] J. Walsh and E. W. Gill, "An analysis of the scattering of high-frequency electromagnetic radiation from rough surfaces with application to pulse radar operating in backscatter mode," *Radio Science*, vol. 35, no. 6, pp. 1337–1359, 2000.

[22] J. Walsh, J. Zhang, and E. W. Gill, "High-frequency radar cross section of the ocean surface for an FMCW waveform," *Oceanic Engineering, IEEE Journal of*, vol. 36, no. 4, pp. 615–626, Oct 2011.

[23] D. Barrick, "First-order theory and analysis of mf/hf/vhf scatter from the sea," *Antennas and Propagation, IEEE Transactions on*, vol. 20, no. 1, pp. 2–10, Jan 1972.

[24] A. López, G. Segovia, R. Valencia, and E. Valencia, "Study of high frequency surface wave radar (HFSWR)," *Rev. ciênc. exatas, Taubaté*, vol. 11, no. 2, pp. 111–120, 2005.

[25] K. Norton, "The propagation of radio waves over the surface of the earth and in the upper atmosphere," *Proceedings of the Institute of Radio Engineers*, vol. 24, no. 10, pp. 1367–1387, Oct 1936.

[26] L. Andrews, *Special Functions of Mathematics for Engineers*, ser. Oxford science publications. SPIE Optical Engineering Press, 1992.

[27] A. Sommerfeld, "The propagation of waves in wireless telegraphy," *Ann. Phys.*, vol. 28, pp. 665–736, 1909.

[28] D. Barton, *Modern Radar System Analysis*, ser. Artech House Radar Library. Artech House, 1988.

[29] R. Ross, "Radar cross section of rectangular flat plates as a function of aspect angle," *Antennas and Propagation, IEEE Transactions on*, vol. 14, no. 3, pp. 329–335, May 1966.